Food & Function

ROYAL SOCIETY OF CHEMISTRY

PAPER

View Article Online
View Journal | View Issue

Cite this: *Food Funct.*, 2025, **16**, 3671

Curcumin exerts anti-tumor activity in colorectal cancer *via* gut microbiota-mediated CD8$^+$ T Cell tumor infiltration and ferroptosis†

Hongli Zhou, ‡[a,b] Yupei Zhuang,‡[a,b] Yuwei Liang,[a,b] Haibin Chen,[a] Wenli Qiu,[a,c] Huiqin Xu*[a] and Hongguang Zhou*[a,b]

Colorectal cancer (CRC), as a high-incidence malignancy, continues to present significant challenges in prevention, screening, and treatment. Curcumin (Cur) exhibits notable anti-inflammatory and anticancer properties. Despite its poor solubility in water and low bioavailability, high concentrations of Cur are detected in the gastrointestinal tract after oral administration, suggesting that it may directly interact with the gut microbiota and exert regulatory effects. This study aims to explore the mechanisms by which Cur improves CRC by modulating gut microbiota. Firstly, we evaluated the effect of Cur on CRC cell viability *in vitro* using the MTT assay, and the results showed a significant inhibitory effect on CRC cell growth. The IC50 values for Cur in CT26 and RKO cells were 23.52 μM, 16.11 μM, and 13.62 μM at 24, 48, and 72 hours, respectively, and 26.3 μM, 16.52 μM, and 14.22 μM at 24, 48, and 72 hours, respectively. Cur induced apoptosis and caused G2 phase cell cycle arrest in tumor cells. Subsequently, we established a CRC mouse model. Oral administration of Cur at 15 mg kg^{-1} and 30 mg kg^{-1} inhibited CRC progression, as evidenced by reduced tumor volume, histological analysis, immunohistochemistry, and an increased number of CD8$^+$ T cells infiltrating the tumors. Ferroptosis in tumor cells was also observed. Cur partially restored the gut microbiota of CRC mice, altering the abundance and diversity of the gut microbiota and affecting serum metabolite distribution, with significant increases in the abundance of SCFA-producing microbes such as *Lactobacillus* and *Kineothrix*. To verify causality, we designed a fecal microbiota transplantation (FMT) experiment. Compared with CRC mice, the fecal microbiota from Cur-treated mice significantly alleviated CRC symptoms, including slowed tumor growth, enhanced CD8$^+$ T cell tumor infiltration, and induced ferroptosis in tumor cells. Additionally, when gut microbiota was depleted with antibiotics, Cur's antitumor effects disappeared, suggesting that Cur mitigates CRC in a gut microbiota-dependent manner. These findings provide new insights into the mechanisms underlying CRC and propose novel therapeutic interventions, emphasizing the interaction between gut microbiota and immune responses within the tumor immune microenvironment (TIME).

Received 21st August 2024,
Accepted 2nd April 2025

DOI: 10.1039/d4fo04045g

rsc.li/food-function

1. Introduction

Colorectal cancer (CRC) is one of the most common malignant tumors worldwide. According to the latest epidemiological studies, in 2023, approximately 153 020 people globally were diagnosed with CRC, of which 52 550 died from the disease.[1] Over the past few decades, both the incidence and mortality rates of CRC have been increasing globally, especially in low and middle Social Development Index countries in Asia and Africa.[2] In the Asian region, the epidemiology of CRC shows some unique trends. The latest research indicates that Asia had the highest global rates of CRC incidence (51.8%) and mortality (52.4%), which are associated with Westernized dietary habits, an aging population, smoking, lack of physical exercise, and other risk factors.[3] CRC's etiology and pathogenesis are multifaceted, encompassing genetic, environmental, and inflammatory factors. Genetic predispositions such as familial and hereditary factors play a critical role. Moreover, lifestyle and ecological factors significantly contribute to its onset.[4] The inflammatory aspect of its pathogenesis has also

[a]*Nanjing University of Chinese Medicine, 210023, Nanjing, China. E-mail: 260105@njucm.edu.cn, 300008@njucm.edu.cn*
[b]*Jiangsu Collaborative Innovation Center of Traditional Chinese Medicine in Prevention and Treatment of Tumor, 210023 Nanjing, China*
[c]*Department of Radiology, Affiliated Hospital of Nanjing University of Chinese Medicine, 210023 Nanjing, China*

†Electronic supplementary information (ESI) available. See DOI: https://doi.org/10.1039/d4fo04045g

‡These authors contributed equally to this work.

been underscored, linking chronic inflammation to CRC development.[5] Current treatment modalities primarily include surgery, chemotherapy, and radiation therapy. Early detection significantly enhances prognosis; however, the disease often presents no typical clinical manifestations, rendering early diagnosis challenging. However, there are limitations to the current treatment approaches. Chemotherapy, a cornerstone of treatment, often proves ineffective due to the disease's inherent resistance mechanisms. Despite advancements, the multifactorial nature of CRC complicates the development of comprehensive treatment strategies, necessitating a multidisciplinary approach encompassing genetic, environmental, and lifestyle modifications alongside medical interventions. Globally, the prevention, screening, and treatment of CRC still face many challenges, requiring collective efforts from the international community to address them.

Recent advancements in cancer management have increasingly investigated the potential role of dietary phytochemicals in regulating health and disease. Curcumin (Cur), a natural polyphenolic compound extracted from turmeric (*Curcuma longa*), is widely used in traditional Indian and Chinese medicine to address various ailments. As the main active component of turmeric, Cur is not only an essential seasoning in Asian cuisine but also extensively studied for its pharmacological properties, including immunomodulation,[6] antioxidation,[7] anti-inflammatory effects,[8] and potential anticancer activity.[9] As the primary source of Cur, turmeric has been used for centuries in traditional medical systems like Ayurveda, Traditional Chinese Medicine, Unani, and Siddha to treat a range of diseases, including inflammatory bowel disease (IBD),[10] liver diseases, and neurodegenerative diseases.[11] Notably, Cur accumulates in the gastrointestinal tract after oral administration, leading to the hypothesis that it may exert part of its biological effects by directly influencing the gut microbiota, which may explain its extensive biological activity despite low systemic bioavailability.[11] Previous studies have shown that Cur and its metabolites impact the composition and activity of the gut microbiota.[12,13] However, it is important to recognize that both diet and cancer involve complex, multifactorial interactions. Therefore, this study does not claim that curcumin has broad or definitive anticancer or preventive effects but focuses on exploring its acute cellular effects. Through this approach, we aim to investigate the immediate interactions between Cur, tumor cells, and their microenvironment, providing a more targeted perspective that reflects the complex interactions between dietary components and cancer progression.

For the past few years, numerous studies have revealed that dysbiosis of gut microbiota is an indispensable factor correlated to CRC, besides genetic, diet, and other environmental factors.[14–16] It plays a critical role in both the metabolic and immune systems. An increased abundance of certain commensal intestinal bacteria, including *Fusarium oxysporum*, *Escherichia coli*, *Bacteroides fragilis*, and *Enterococcus faecalis*, was observed in CRC tissue. Meanwhile, the relative abundance of bacteria potentially associated with cancer suppression, such as *Roseburia*, *Clostridium*, and *Bifidobacterium*, was reduced. Studies have suggested that these bacteria may influence CRC progression through their metabolites or interactions with the host.[17–20] However, the precise mechanisms underlying these effects require further investigation. The relationship between metabolism and CRC onset, progression, and treatment is also multidimensional and has been a focal point of recent research. Metabolic reprogramming is identified as a hallmark of CRC, with CRC cells and intestinal stem cells (ISCs) adapting their metabolism for rapid proliferation, especially in nutrient-poor environments.[21] A positive association between metabolic syndrome (MetS) and the onset age of early-stage CRC has been observed.[22] Environmental factors, particularly diet, play a pivotal role in CRC pathogenesis by influencing the metabolism of ISCs and promoting metabolic adaptations that support CRC tumorigenesis.[21] A deeper understanding of the mechanistic links between environmental factors, metabolic adaptations, and the tumor microenvironment (TME) holds promise for improved prevention and treatment strategies. Emerging evidence highlights the potential of targeting metabolic pathways for therapeutic intervention, thus opening avenues for more effective treatment strategies.[21] Furthermore, the tumor immune microenvironment (TIME) in CRC is a complex interface where tumor cells interact with the immune system, significantly impacting disease progression and therapy responses. Tumor-Infiltrating Lymphocytes (TILs), including cytotoxic T cells, are a vital component of the TIME in CRC. Their presence often correlates with a better prognosis and response to immunotherapy.[23] Understanding the intricate interactions between T lymphocytes, and other components of the TIME is fundamental for devising targeted immunotherapeutic strategies. The categorization of CRC based on TIL presence has prognostic value, potentially guiding more personalized immunotherapy approaches.[24,25]

The interaction of Cur with the gut microbiota leads to two distinct outcomes: firstly, Cur exerts a direct regulatory effect on the intestinal microflora; secondly, the gut microbiota metabolizes Cur, resulting in the production of active metabolites.[26,27] These two processes are vital for the efficacy of Cur. The use of "omics" technologies, including lipidomic, transcriptomics, metagenomics, and metabolomics, has contributed to understanding the mechanisms that underlie various diseases.[28,29] Multi-omics joint analysis is a sinnvoll for elucidating the pathomechanism of diseases and therapeutic effects. Thus, we examined the gut microbiota and changes in serum metabolites. Subsequently, the improvement of the immune microenvironment in CRC mice by Cur is investigated. By examining the infiltration of $CD8^+$ T cells in the tumor, and the secretion of cytokines, the mechanisms of Cur in treating CRC are explored. Finally, our findings were validated through fecal microbiota transplantation (FMT) experiments. Through this approach, the research aims to unveil the potential antitumor mechanisms of Cur, providing a foundation for future clinical applications.

2. Materials and methods

2.1. Cell culture and drug preparation

CT26 cells and RKO cells were originaly purchased from the Hunan Fenghui Biotechnology Co., Ltd (Fenghbio, CL0077; CL0516). CT26 and RKO cells were cultured in RPMI-1640 (Keygenbio, KGL1503-500), supplemented with 10% FBS (Keygenbio, KGL3002-500) and 1% Penicillin–Streptomycin (Keygenbio, KGL2303-100). All cell lines were cultured in a humid at mosphere of 5% carbon dioxide-95% air at 37 °C. The cells were harvested using trypsin-EDTA solution (Keygenbio, KGL2101-100) when reaching 70–80% confluency. Oxaliplatin and Cur were purchased from Shanghai Yuanye Biotechnology Co., Ltd (Yuanye, B83134; S31628). Cur was dissolved in DMSO to create a 40 mM stock solution, which was stored at −80 °C for future use. In cell culture experiments, the Cur stock solution was diluted to the required concentration with the culture medium. Oxaliplatin was dissolved in the culture medium and freshly prepared for each use, with the DMSO concentration in the Oxaliplatin solution matched to that in theCur treatment groups. For animal experiments, Cur was prepared as a suspension in a 1% sodium carboxymethyl cellulose (CMC) solution (Sigma-Aldrich, 419273). In accordance with clinical standards for Oxaliplatin administration, Oxaliplatin was dissolved in 5% dextrose injection.

2.2. Growth inhibition studies

CT26 cells and RKO cells were seeded into 96-well plates at a density of 8×10^3 cells per well and cultured in the standard condition. Then, the cells were treated with varying concentrations (0.5, 1, 5, 10, 50, 100 μM) of Cur for 24, 48, and 72 h, followed by an assessment of cell viability with an MTT assay kit (Keygenbio, KGA9301-1000), in light of the manufacturer's protocol. Absorbance readings were taken at a wavelength of 490 nm on amicroplate reader. To ensure that the observed effects were attributed to Cur itself rather than the influence of the solvent DMSO, a control group was included in the experiment. Cells in the control group were treated with the same concentration of DMSO as in the Cur-treated group (final DMSO concentration ≤0.1%, a concentration that has been demonstrated in previous studies to have no impact on normal cell growth).[30,31] This setup was used to evaluate the potential effects of DMSO on cell viability and other parameters.

2.3. Cell cycle analysis

CT-26 and RKO cells were seeded overnight in a six-well plate with culture medium, then treated with Cur (5 μM and 10 μM) and oxaliplatin (10 μM) for 48 hours to analyze cell cycle distribution. All drugs were diluted in culture medium. Cells in the control and oxaliplatin groups were treated with the same concentration of DMSO as in the Cur-treated group to ensure experimental consistency. Oxaliplatin, a known DNA-damaging agent that induces cell cycle arrest,[32] was used as a positive control. It was used to validate the gating strategy and confirm the expected distribution of cells across different cell cycle phases after treatment. Following the cell cycle kit instructions (Elabscience, E-CK-A351), cell pellets were fixed overnight at 4 °C in 70% cold ethanol, then incubated with RNase at 37 °C for 30 minutes. Finally, cell nuclei were stained with propidium iodide (PI) for 30 minutes. Cell cycle distribution was analyzed using a CytoFLEX-2 flow cytometer and FlowJo software.

2.4. Cell apoptosis analysis

To analyze the cell apoptosis, CT-26 cells and RKO cells were seeded in a six-well plate overnight in normal growth media and then treated with Cur (5 μM and 10 μM) and oxaliplatin (10 μM) for additional 48 h. Cells in the control group were treated with the same concentration of DMSO as in the Cur-treated group. All drugs were diluted in the culture medium. After cell treatment, cells were collected and resuspended. Annexin V FITC/PI reagent (Elabscience: E-CK-A211) was added, and apoptosis was detected using a flow cytometer (CytoFLEX-2, Beckman). Data were analyzed using FlowJo software.

2.5. Experimental animals

Healthy specific pathogen-free BALB/c male mice (18–22 g, 6 weeks old) were purchased from Hangzhou Medical College, with certificate number SCXK(Zhe) 2019-0002, and fed in the Animal Laboratory Center and provided with food and water freely under standard conditions (temperature between 23 °C and 27 °C and lighting regimen of 12 h light/dark) for 7-day acclimatization. The animal research procedure received approval from the Ethics Committee of Nanjing University of Chinese Medicine (202309A001) and adhered to the laboratory animal guidelines stated in the Declaration of Helsinki. For administration, Cur was dissolved in a 1% sodium carboxymethyl cellulose solution.[33] Cur exhibits significant anti-tumor activity in CRC. Previous studies have demonstrated that administering Cur to mice at doses of 25 mg kg^{-1} or 30 mg kg^{-1} shows significant anti-CRC efficacy.[34,35] Therefore, based on established dosage ranges, we selected 15 mg kg^{-1} and 30 mg kg^{-1} dose groups to investigate the anti-CRC mechanisms of Cur, and conducted toxicological experiment. Oxaliplatin was prepared in a 5% w/v Glucose Solution.

As shown in Fig. 2A, to create a subcutaneous CT26 CRC model, CT26 cells were diluted in RPMI 1640 solution (1×10^6 cells per mouse) and injected beneath the skin in the right groin of the mice. After 5 days, the mice were divided into 5 groups randomly, with each group consisting of 7 mice: (1) Control group: normal BALB/c mice without inoculation of CT26 cells, but they were given a 1% CMC-Na gavage; (2) Model group: mice received an injection of CT26 cells, but instead of the experimental treatment, they were given a 1% CMC-Na gavage; (3) Oxaliplatin group: treated with the oxaliplatin at a dosage of 5 mg kg^{-1} every 3 days; (4) Low dose group of Cur (Cur-L): treated with the Cur at a dosage of 15 mg kg^{-1}; (5) High dose group of Cur (Cur-H): treated with the Cur at a dosage of 30 mg kg^{-1}. The volume of the tumor was computed using the equation: volume = length × width2 × 0.5 and monitored every 3 days by Vernier calipers. All groups ofmice

were administered treatment for 16 days after successful modeling, and the mice were sacrificed for sample collection 2 hours after the final dose. Cur was administered *via* oral gavage at a dosing volume of 0.2 ml per 10 g. Oxaliplatin was administered *via* intraperitoneal injection at a dosing volume of 0.1 ml per 10 g. The control and model groups were given 1% CMC-Na at the same volume as the treatment groups.

As shown in Fig. 2E, the orthotopic tumor model was established as follows: Firstly, a subcutaneous tumor model was established using one male BALB/c mouse. When the tumor volume reached 500 mm^3, the mouse was euthanized, the mouse was executed, and the skin was sterilized with 75% ethanol, the subcutaneous tumor was peeled off and immersed in saline containing penicillin and streptomycin, the surrounding connective tissues were removed, and the tissues where the tumor growing vigorously were taken, and the tumor was shredded into 1 mm × 1 mm × 1 mm lumps for spare use. After anesthesia, the mice were fixed supine and the abdominal operation area was sterilized with 75% ethanol. A small incision of approximately 1 cm was made in the left lower abdomen to reveal the cecum, which was dragged out to the skin. A small amount of plasma membrane at the junction of the cecum and colon was gently scraped off with a 4-gauge needle, and after a slight oozing of blood, the prepared mass was glued to the scrape with medical tissue adhesive and dried for 10 seconds. The cecum was inserted into the abdomen, and the abdominal wall was sutured (mice in the sham surgery group underwent the same procedure up to this step without tumor implantation). After 5 days of acclimatization, a solid abdominal bulge of about 2–3 mm was observed, indicating successful modeling and the whole process was carried out following the principle of aseptic operation. After 5 days, the mice were divided into 5 groups randomly, with each group consisting of 7 mice, including the control group (sham surgery group), the model group, the oxaliplatin group, the Cur-H (30 mg kg^{-1}) group, and the Cur-H (15 mg kg^{-1}) group. All groups of mice were administered the treatment starting from day 5, and the mice were sacrificed for sample collection 2 hours after the final dose, with a total treatment duration of 16 days. The administration methods were consistent with those used in the aforementioned subcutaneous CT26 CRC model.

2.6. Histopathology and immunohistochemistry

Upon concluding the experiment, tumor tissues from mice were harvested, fixed in 4% paraformaldehyde for 48 hours, and subsequently dehydrated and embedded in paraffin. The tissues were sectioned and stained with hematoxylin and eosin (H&E) for morphologic analysis under a light microscope. Following this, the tissues were dewaxed and subjected to heat-induced antigen retrieval in citrate buffer (pH 6.0), before incubation with Ki-67 (Servicebio, GB111141-100, 1 : 600) primary antibodies. Post an overnight incubation at 4 °C, the slides were rinsed with phosphate-buffered saline (PBS), then incubated with a secondary antibody (Servicebio, GB23301) for 30 minutes at room temperature, and stained with a DAB substrate kit (Servicebio, G1212-200T). Visualization of the stained samples under a microscope at ×40 magnification followed. For each slide, three fields of view were randomly selected, and ImageJ software was employed to calculate the average percentage of positively stained cells within each field.

2.7. Flow cytometry

Excised tumors were placed in a 100 mm culture dish and immediately treated with 5–10 ml of HBSS at room temperature. The volume of each tumor did not exceed 1000 mm^3, with weights ranging from 0.6 to 0.8 g. Once all tumors were harvested, they were transferred into 1.5 ml Eppendorf tubes and minced using curved scissors. The minced tissue was then transferred into a 50 ml centrifuge tube, and a digestion solution composed of collagenase type IV (0.2 mg mL^{-1}) (Biosharp, BS165-1 g), hyaluronidase (0.2 mg mL^{-1}) (Biosharp, BS171-100 mg), and deoxyribonuclease I (0.1 mg mL^{-1}) (Biosharp, BS137-10 mg) was added to facilitate tissue breakdown at 37 °C, 80 rpm for one hour. Post-digestion, the suspension was centrifuged at 1500 rpm for 5 minutes, the supernatant was discarded, and the pellet was resuspended in 10 ml HBSS. This suspension was transferred to a 15 ml centrifuge tube and subjected to a second centrifugation at 1500 rpm for 5 minutes. Cells were then resuspended in 40% Percoll (Biosharp, BS909-100 ml) and carefully layered over 4 ml of 80% Percoll pre-added in a new 15 ml centrifuge tube. After centrifugation at 1500 rpm for 30 minutes (acceleration set to 1 and deceleration to 0), immune cells were collected at the interphase between 40% and 80% Percoll. The cells were washed with PBS, resuspended in 100 μl PBS, and transferred to a new 1.5 ml Eppendorf tube for subsequent staining. Isolated immune cells were stained using a Zombie NIR™ Fixable Viability Kit (Biolegend, 423106), anti-CD45-PE/Cyanine7 (Biolegend, 157205), anti-CD3-FITC (Biolegend, 100204), and anti-CD8a-APC (Biolegend, 100712). The cellular composition was then analyzed using a flow cytometer (CytoFLEX-2, Beckman) to determine the percentage of each cell type.

2.8. Immunofluorescence staining

Immunofluorescence staining was performed to observe the expression of $CD3^+$, $CD4^+$, and $CD8^+$ T cells. The TSA, primary and secondary antibodies used in this experiment were as follows: Anti-CD3 Rabbit pAb (Servicebio, GB111337-100, 1 : 700), An-ti-CD4 Rabbit pAb (Servicebio, GB11064-100, 1 : 700), Anti-CD8 Rabbit pAb (Servicebio, GB114196-100, 1 : 700), HRP-conjugated goat anti-rabbit IgG (Servicebio, GB23303, 1 : 500), CY3-Tyramide (Servicebio, G1223, 1 : 500), iF647-Tyramide (Servicebio, G1232, 1 : 500), iF488-Tyramide (Servicebio, G1231, 1 : 500). The fluorescent signals were observed with a high-resolution digital slide scanner (Pannoramic MIDI, 3DHISTECH, Hungary).

2.9. ELISA

The serum concentrations of IFN-γ, TNF-α, and IL-2 were determined using ELISA kits (Elabscience, E-EL-M0048c,

E-EL-M3063, and E-MSEL-M0036) according to the manufacturer's instructions. The concentrations of MDA, SOD, and GSH were determined using the Assay Kits (Elabscience, E-BC-K025-M, E-BC-K020-M, and E-BC-K030-M) according to the manufacturer's instructions.

2.10. Western blotting analysis

Tumor tissues were washed 2–3 times with pre-cooled PBS, minced, and placed in homogenization tubes with two 4 mm homogenization beads. Ten volumes of lysis buffer (Servicebio, G2002-100ML) were added, and homogenization was carried out using a preset program. Following homogenization, the mixture was incubated on ice with lysis buffer for 30 minutes, with vortexing every 5 minutes to ensure complete tissue lysis. Subsequently, the homogenate was centrifuged at 12 000 rpm, 4 °C for 10 minutes, and the supernatant containing total protein was collected. Protein concentration in the samples was determined using the BCA method (Servicebio, G2026). A total of 20 μg of protein from the tissue lysate was separated on a 10% SDS-PAGE gel and transferred to a polyvinylidene fluoride membrane for 1 hour. The membranes were blocked with 5 percent (w/v) non-fat dry milk in TBST buffer for 1 hour at 25 °C and then incubated overnight at 4 °C with primary antibodies against GPX4 (Servicebio, GB124327, 1 : 1000), SLC7A11 (Servicebio, GB115276, 1 : 1000), ACTIN (Servicebio, GB15001, 1 : 2000), CXCR3 (Proteintech, 26756, 1 : 1000), and CXCL10 (Proteintech, 10937, 1 : 1000), followed by co-incubation with HRP-labeled secondary antibodies (Servicebio, GB23301).

2.11. 16S rRNA sequencing

Fecal samples were collected from mice by gently stimulating the anus using sterile tweezers, and 2–3 pellets were obtained per mouse. Samples were immediately transferred to sterile 1.5 mL Eppendorf tubes, flash-frozen in liquid nitrogen for 30 minutes, and stored at −80 °C until DNA extraction.

Total DNA was extracted from fecal samples using the E.Z.N.A.® Soil DNA Kit (Omega Bio-tek, USA) following the manufacturer's instructions. The V1–V9 region of the 16S rRNA gene was amplified using primers 27F (5′-barcode-AGAGTTTGATCMTGGCTCAG-3′) and 1492R (5′-CRGYTACCTTGTTACGACTT-3′). Amplicons were purified and quantified using a Qubit® 3.0 fluorometer (Invitrogen, USA), normalized, and pooled. SMRTbell libraries were constructed through DNA repair, end-repair, and adapter ligation. Sequencing was performed on the PacBio Sequel IIe platform, generating high-quality reads through real-time fluorescence signal detection. Raw sequencing data were processed using the DADA2 algorithm to denoise and generate amplicon sequence variants (ASVs). Sequence length distributions were examined to ensure consistency with expected amplicon sizes, and abnormal sequences were excluded. ASVs were aligned to the SILVA 16S rRNA database (v138) using RDP Classifier (v2.2) and the uclust algorithm. Taxonomic profiles were generated for each sample at the phylum, class, order, family, genus, and species levels. Alpha diversity indices, including Observed species, Shannon, and PD_Faith, were calculated to evaluate species richness and evenness. PD_Faith quantified phylogenetic diversity based on evolutionary distances. Principal coordinate analysis (PCoA) was used to assess differences in community composition among samples based on non-Euclidean distances. LefSe analysis was conducted to identify significantly different taxa between groups using the Kruskal–Wallis rank sum test and linear discriminant analysis (LDA) to evaluate the effect size of differentially abundant taxa. And Bioinformatic analysis was performed using the OECloud tools at **https://cloud.oebiotech.com**.

2.12. Metabolomic analysis

The samples, initially stored at −80 °C, were thawed at room temperature. Next, 80 μL of serum was transferred to a 1.5 mL tube. A 240 μL mixture of methanol and acetonitrile (2 : 1, vol/vol) was added and vortexed for 1 minute. Ultrasonic extraction was then performed in an ice-water bath for 10 minutes. The solution was centrifuged at 4 °C (13 000 rpm) for 10 minutes, and 200 μL of the supernatant was carefully collected and transferred to a glass vial for drying in a freeze-concentration centrifugal dryer. Each sample was treated with 300 μL of a methanol–water mixture (1 : 4, vol/vol) and vortexed for 30 seconds. Another ultrasonic extraction was performed in an ice bath for 3 minutes. The mixture was then centrifuged at 4 °C (13 000 rpm) for 10 minutes, and 150 μL of the supernatant from each tube was filtered through a 0.22 μm microfilter and transferred to an LC vial. The specimens were stored at −80 °C until LC-MS analysis. The QC sample was prepared by amalgamating individual samples into a composite mixture.

Separation was performed using a Hypesil Gold column (100 × 2.1 mm, 1.9 μm) with a flow rate of 0.2 mL min^{-1}. The mobile phase consisted of 0.1% formic acid in water (solvent A) and acetonitrile (solvent B), with the following gradient program: 0–3 minutes, 5%–45% B; 3–13 minutes, 40%–95% B; 13–14 minutes, 95% B; 14–15 minutes, 95%–5% B. Mass spectrometry was performed in both positive and negative ionization modes under optimized settings. In positive ion mode, the conditions were as follows: ion source temperature of 100 °C, capillary voltage of 2.5 kV, cone voltage of 24 V, desolvation gas flow rate of 800 L h^{-1}, and cone gas flow rate of 50 L h^{-1}. In negative ion mode, the ion source temperature was 100 °C, with a capillary voltage of 2.5 kV, cone voltage of 25 V, desolvation gas flow rate of 600 L h^{-1}, and cone gas flow rate of 10 L h^{-1}. The mass spectrometry scan covered a range of 50–1500 Da for product ion scanning and 100–2000 Da for TOF-MS analysis.

The original data were analyzed using MarkView™ software. Orthogonal partial least squares-discriminant analysis (OPLS-DA) was performed using metaX to visualize sample clustering across different groups. Metabolites with a variable importance in projection (VIP) score >1 and a p-value <0.05 were identified as differential metabolites. Potential biomarkers and metabolic pathways were further identified using the HMDB Database (**https://www.hmdb.ca/**), METLIN Database (**https://metlin.scripps.edu/**), MassBank Database (**https://www.massbank.jp/**), and KEGG Database (**https://www.genome.jp/kegg/**).

2.13. Fecal microbiota transplantation

A broad-spectrum antibiotic (ABX) cocktail (ampicillin 1 g L^{-1}, Macklin, A6265-500 g; neomycin sulfate 1 g L^{-1}, Macklin, N6063-100 g; metronidazole 1 g L^{-1}, Macklin, M813525-25 g; vancomycin 0.5 g L^{-1}, Macklin, V871983-100 g) was administered orally in sterile water for 2 weeks prior to FMT to establish a pseudo-germ-free mouse model.[36] The orthotopic tumor model was constructed following the procedure described in section 2.5. After 5 days of acclimatization, a solid abdominal bulge of approximately 2–3 mm was observed, indicating successful modeling. The entire process was carried out under aseptic conditions. For FMT, 15 healthy specific pathogen-free male BALB/c mice (18–22 g, 6 weeks old) were divided into 3 groups of 5 mice each: the model group (oral gavage with saline), the M-FMT group (receiving fecal microbiota transplantation from the model group), and the C-FMT group (receiving fecal microbiota transplantation from the Cur-H group). During the FMT period, 10 mice were selected as donor mice and were not treated with antibiotics. After modeling, the mice were divided into two groups of 5 mice each: one group served as fecal donors for the M-FMT group and the other for the C-FMT group. The fecal donor mice in the M-FMT group were gavaged with 1% CMC-Na, while those in the C-FMT group were treated with Cur at a dosage of 30 mg kg^{-1}. Fresh feces were collected daily from CRC mice and mice after Cur gavage under aseptic conditions. For every 0.1 g of feces, 1 mL of saline was added, homogenized for 10 minutes, and then centrifuged at 1000 rpm for 3 minutes. The precipitate was discarded, and the supernatant collected. The supernatant was used for gavage. CRC mice were gavaged with 0.2 mL of FMT solution per mouse daily for 16 days. FMT was performed 12 hours after gavage in the donor mice to minimize residual drugs in the feces.

2.14. Gut microbiota depletion

10 healthy SPF male BALB/c mice (18–22 g, 6 weeks old) were divided into two groups of five mice each: the ABX + CMC group (oral gavage with 1% CMC-Na) and the ABX + Cur group (treated with Cur at a dosage of 30 mg kg^{-1}). Mice were treated with the ABX cocktail for 14 days before Cur treatment to deplete their gut microbiota (as described in section 2.12). The orthotopic tumor model was constructed as described in section 2.5. Tumor volume was calculated using the equation: volume = length × $width^2$ × 0.5 and monitored every 3 days with Vernier calipers. All groups of mice received treatment for 16 days after successful tumor modeling, and were sacrificed for sample collection 2 hours after the final dose. Cur was administered *via* oral gavage at a dose of 0.2 mL per 10 g. The ABX + CMC group was given 1% CMC-Na at the same volume as the ABX + Cur group.

2.15. Correlation analysis

The correlation between the relative abundance of microbial genera and the response intensity data of corresponding metabolites was calculated based on the sample correspondence. Pearson Correlation Analysis was used for data processing. Bioinformatic analysis was performed using the OECloud tools at **https://cloud.oebiotech.com**.

2.16. Statistics analysis

Data analysis was performed using SPSS 27.0 software for statistical analysis and GraphPad Prism 9.0 software for graphing. For comparisons between two groups of continuous data, normality tests were first conducted. If both groups met the normality assumption, an unpaired t-test was used for comparison; otherwise, the non-parametric Wilcoxon rank-sum test was used. Similarly, for comparisons among multiple groups of continuous data, if the data were normally distributed, one-way ANOVA was performed, followed by *post-hoc* pairwise comparisons using the Bonferroni method if significant differences were found. If the data were not normally distributed, the Kruskal–Wallis rank-sum test was used for group comparisons, with subsequent pairwise comparisons conducted using the Dunn's test for multiple comparisons if significant differences were observed. A two-sided P-value <0.05 was considered statistically significant.

3. Results

3.1. Cur inhibits the proliferation of CRC cells, induces apoptosis, and causes cell cycle arrest

To investigate the effects of Cur on CRC cells, we first examined the impact of different concentrations of Cur (0.5, 1, 5, 10, 50, 100 μM) on the proliferation of mouse CRC CT26 cells and human CRC RKO cells. The MTT assay results demonstrated that Cur inhibited cell viability at 24, 48, and 72 h in a concentration- and time-dependent manner (Fig. 1A and B). The IC_{50} values of Cur for CT26 cells after 24, 48, and 72 h of treatment were 23.52, 16.11, and 13.62 μM, respectively (Fig. 1C). Similarly, for RKO cells, the IC_{50} values after 24, 48, and 72 hours of treatment were 26.30, 16.52, and 14.22 μM, respectively (Fig. 1D). Therefore, to ensure cytotoxicity without causing excessive cell death that could affect experimental outcomes, two doses below the IC_{50} values (5 μM and 10 μM) were selected for apoptosis and cell cycle experiments, and measurements were taken after 48 h of treatment. Compared with the control group, Cur significantly induced apoptosis in CT26 and RKO cells in a concentration-dependent manner. As a positive control, oxaliplatin also significantly induced apoptosis in CT26 and RKO cells *in vitro* (Fig. 1E and F). Additionally, Cur was found to block tumor cells in the G2 phase, thereby inhibiting tumor cell proliferation and ultimately leading to apoptosis (Fig. 1G and H).

3.2. The impact of Cur on tumor growth in CRC mouse

Firstly, we established subcutaneous and orthotopic CRC models to evaluate the inhibitory effects of Cur on tumor growth (Fig. 2). In mice administered with Cur or oxaliplatin, tumor progression was impeded, with the groups of oxaliplatin and Cur-H demonstrating enhanced antitumor efficacy.

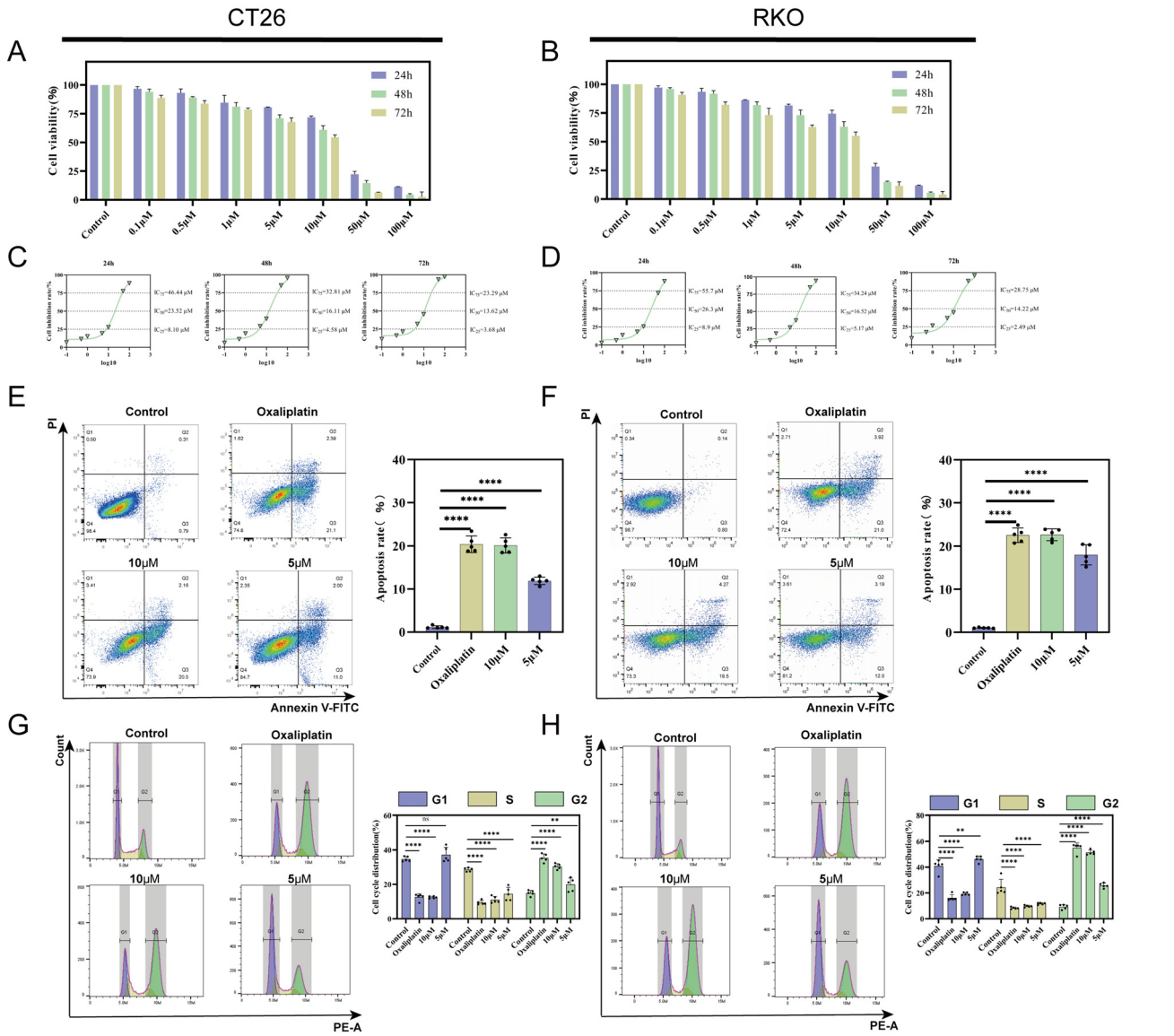

Fig. 1 Cur inhibits the proliferation of CRC cells, induces apoptosis, and causes cell cycle arrest. (A and B) MTT assay of CT26 cells and RKO cells treated with diversified concentrations of Cur for 24, 48, and 72 h. n = 9. (C and D) The IC_{25}, IC_{50}, IC_{75} values after 24, 48, and 72 hours of treatment by Cur. (E and F) Cur significantly induced apoptosis in CT26 and RKO cells in a concentration-dependent manner. n = 5. (G and H) Curcumin causes tumor cells to be arrested in the G2 phase of the cell cycle. n = 5. $^{**}p < 0.01$; $^{****}p < 0.0001$*vs* control group.

Examination of the tumor growth curves indicates a marked deceleration in tumor progression in mice following administration of either Cur or oxaliplatin. Two weeks post-administration, there was a notable decrease in tumor mass in mice from both the Cur-H and oxaliplatin groups compared to the model group (Fig. 2B and F).

In mice post-Cur treatment, necrotic foci were observed in tumor tissues. Within these necrotic areas, tumor cells manifested as structure-less eosinophilic debris, with necrotic cell debris being prevalent. In the model group, cells displayed pronounced atypia and were irregularly arranged. The nuclei were enlarged, and hyperchromatic, with an uptick in nuclear division, and granular chromatin was noted in the model group. Relative to the model group, the Cur and oxaliplatin groups exhibited reduced nuclear division in tumor tissues. Particularly in the Cur-H and oxaliplatin groups, extensive areas of necrosis were observed, harboring a plethora of necrotic cells (Fig. 2C and G). Utilizing immunohistochemistry, we elucidated the expression of Ki-67 within the tumor tissue. Relative to the model group, a notable diminution in Ki-67 expression within the tumor tissue was observed post-treatment, implying that Cur may possess potent antitumor activity (Fig. 2D and H). Additionally, after oral administration of Cur, no abnormalities were observed in the H&E staining of the heart, liver, spleen, lungs, and kidneys of the mice (ESI Fig. S1†). Complete Blood Count (CBC) and liver and kidney function were all within normal ranges, indicating that Cur has a good safety profile at therapeutic doses (ESI Tables S1–S3†).

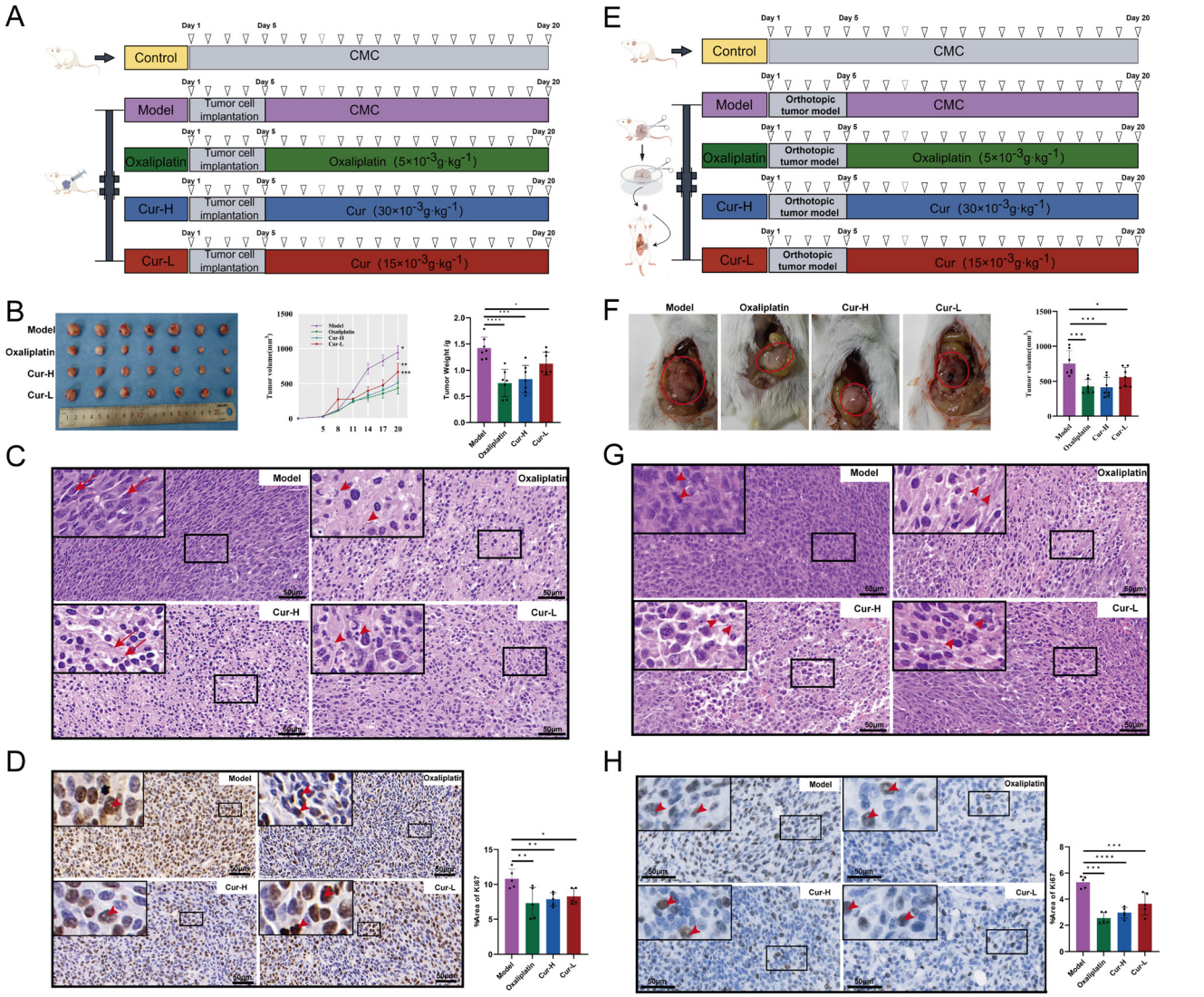

Fig. 2 Anti-tumor efficacy of Cur. (A) Experimental procedure of subcutaneous CT26 CRC model. (B) Tumor volume and tumor weight of different treatment groups (subcutaneous tumor model). (C) H&E of tumor tissues (subcutaneous tumor model). Scale bar = 50 μm. (D) The expression levels of Ki-67 in the tumor tissue were analyzed by immunohistochemistry (subcutaneous tumor model). Scale bar = 50 μm. (E) Experimental procedure of orthotopic tumor model. (F) Tumor volume and tumor weight of different treatment groups (orthotopic tumor model). (G) H&E of tumor tissues (orthotopic tumor model). Scale bar = 50 μm. (H) The expression levels of Ki-67 in the tumor tissue were analyzed by immunohistochemistry (orthotopic tumor model). Scale bar = 50 μm (n = 5–7) *p < 0.05; **p < 0.01; ***p < 0.001; ****p < 0.0001*vs* model group.

3.3. The effects of Cur on the immune microenvironment of CRC

Subsequently, we conducted a detailed analysis of the anti-CRC mechanisms of Cur in the orthotopic CRC model.

Utilizing immunohistochemistry, we elucidated the expression of VEGF and Caspase3 within the tumor tissue. Relative to the model group, a notable diminution in VEGF and Caspase3 expression within the tumor tissue was observed post-treatment (Fig. 3A), indicating that Cur inhibits tumor angiogenesis and induces apoptosis of tumor cells. To evaluate the influence of Cur on the tumor immune microenvironment, we utilized flow cytometry to measure the prevalence of $CD8^+$ T cells in mouse tumor tissues. Fig. 3B showcases a significant increase in the proportion of $CD8^+$ T cells in the Cur group as opposed to the model group (P < 0.01). $CD8^+$ T cells are acknowledged as the primary effector cells in antitumor immunity, their infiltration into the TME being pivotal for cancer cell elimination. The same trend was mirrored in the immunofluorescence analysis of tumor tissues (Fig. 3C), underlining that Cur significantly bolstered the proportion of $CD8^+$ T cells in tumor tissues. This suggests Cur's potential in augmenting the level of killer immune cells *in vivo*. To further examine the impact of Cur on the functionality of $CD8^+$ T cells, we employed ELISA kits to ascertain serum levels of IFN-γ, TNF-α, and IL-2 given that cytokine activation is crucial for their anti-

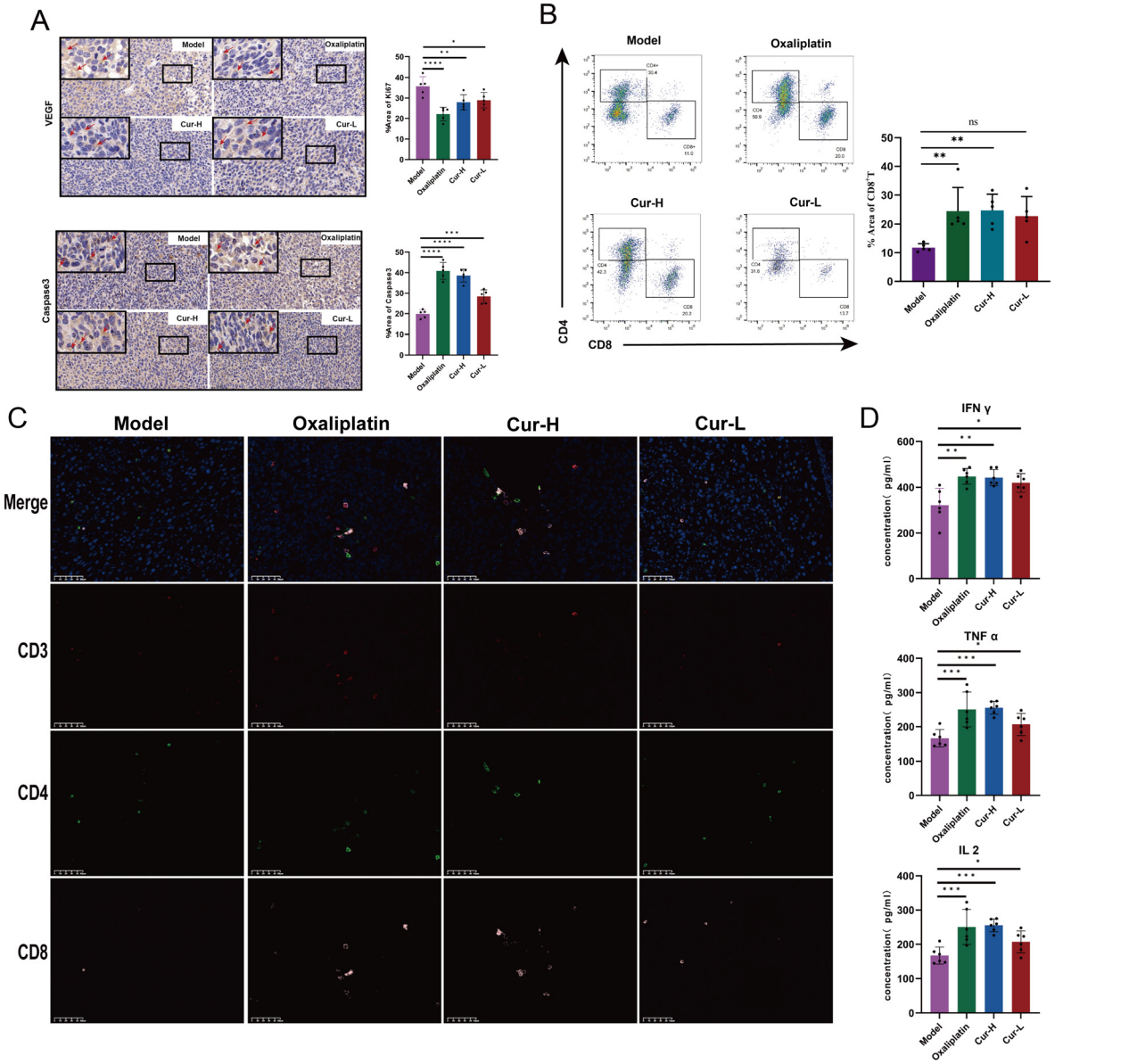

Fig. 3 The effects of Cur on the immune microenvironment of CRC. (A) The expression of VEGF and Caspase3 within the tumor tissues. (B) The expression of $CD8^+$ T cells from tumor tissues. (C) Representative immunofluorescent staining of $CD3^+$, $CD4^+$, and $CD8^+$T cells in tumor tissues. Scale bar = 50 μm. (D) The expression of IFN-γ, IL-2, and TNF-α production in the serum (n = 5–6). *p < 0.05, **p < 0.01, ***p < 0.001; ****p < 0.0001 *vs.* model group.

tumor activities. The ELISA data revealed that CRC mice treated with Cur exhibited increased levels of TNF-α, IFN-γ, and IL-2 in the serum relative to the model group, with this variance being dosage-dependent (Fig. 3D). Thus, we deduce that Cur treatment mitigated the prevalence of immunosuppressive cells while concurrently bolstering T cell-mediated antitumor immunity.

3.4. Cur facilitated the ferroptosis of tumor tissues

Ferroptosis is a distinct, non-apoptotic, iron-dependent form of programmed cell death, characterized by lipid peroxidation and GPX4 dysfunction. $CD8^+$ T cells regulate tumor ferroptosis during cancer immunotherapy. IFN-γ secreted by $CD8^+$ T cells downregulates SLC7A11, inhibiting cystine uptake in tumor cells, thus promoting lipid peroxidation and ferroptosis. We have found that Cur increases $CD8^+$ T cell infiltration and IFN-γ secretion in tumor tissues. To determine whether Cur's effect on $CD8^+$ T cells induces ferroptosis in tumor cells, we examined changes in key ferroptosis indicators in tumor tissues from different mouse groups. Initially, we assessed changes in Iron, SOD, MDA, and GSH levels in tumor tissues. We found that, compared to the model group, SOD and GSH levels decreased in a dose-dependent manner after treatment, particularly in the oxaliplatin and Cur-H groups (Fig. 4A). In

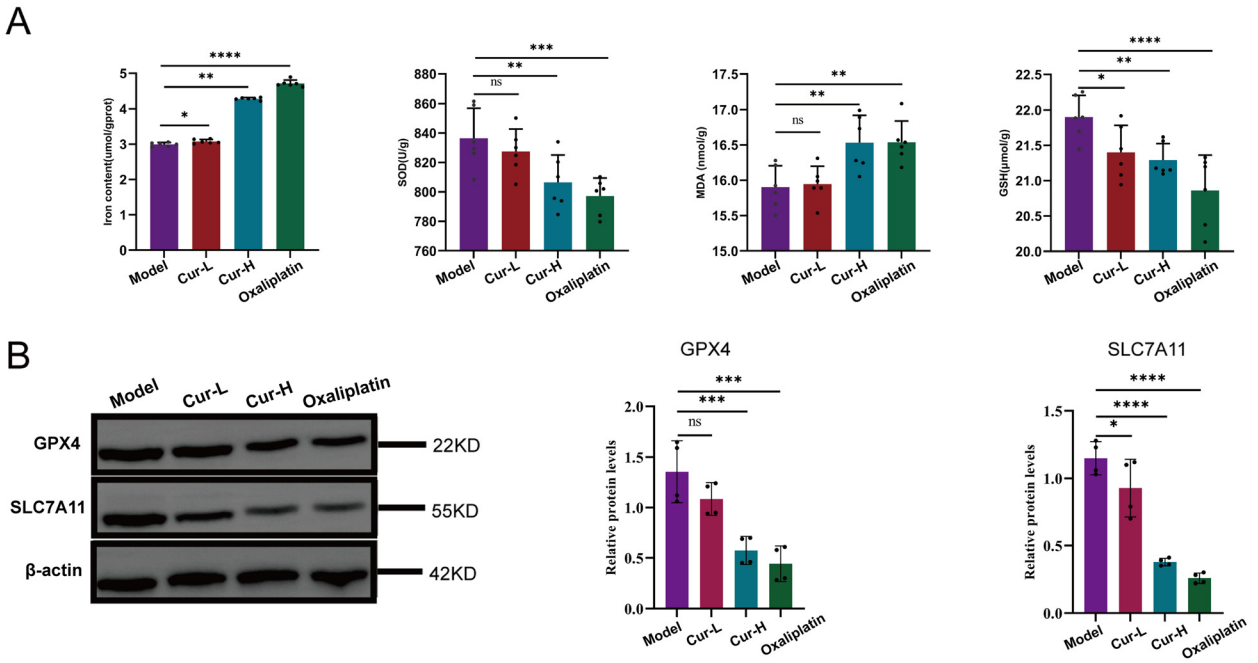

Fig. 4 Cur facilitated the ferroptosis of tumor tissues. (A) The levels of Iron, SOD, MDA, and GSH in tumor tissues. (B) The expression GPX4 and SLC7A11 in tumor tissues (n = 4). *p < 0.05; **p < 0.01; ***p < 0.001; ****p < 0.0001 *vs* model group.

contrast, Iron and MDA levels in tumor tissues significantly increased after treatment (Fig. 4A). We then conducted western blot to detect changes in ferroptosis-related proteins. We observed that Cur significantly reduced GPX4 and SLC7A11 protein expression in tumor tissues (Fig. 4B).

3.5. Effects of Cur on the fecal microbiota of CRC mice

Clinical investigations have demonstrated a dysbiosis of gut microbiota in patients with CRC, with compromised gut microbiota exacerbating the progression of CRC. Consequently, this study evaluated whether the ameliorative effects of Cur on CRC in mice correlate with alterations in the gut microbiome. Alpha diversity, a critical index of microbial composition richness and evenness was assessed. The results indicated significant differences in the Observed species, Pd_faith, and Shannon indices between the Cur group and the model group (P < 0.05), suggesting that continuous administration of Cur for 2 weeks markedly impacts the alpha diversity of the mice gut flora (Fig. 5A, B and C). The rank abundance curves were utilized to arrange the Operational Taxonomic Units (OTUs) in the samples in a specific order based on their relative abundance. These curves, plotted with relative abundance as the ordinate, reflect both species richness (span of the abscissa) and evenness (steepness of the curve). Compared to normal mice, CRC model mice exhibited a trend of reduced species richness and diversity. After the administration of Cur, a noticeable rightward shift was observed in the rank abundance curves (Fig. 5D). Principal Coordinates Analysis (PCoA) is an unconstrained data dimension reduction technique employed to investigate the similarities or differences in community composition among samples. There was a significant disparity in the gut microbial composition among the 3 groups (Fig. 5E and F). A series of bacteria at the genus level, including *Muribaculum*, *Duncaniella*, *Kineothrix*, *Lactobacillus*, and *Ileibacterium* were found to either increase or decrease in the model group, while the changes of these bacteria were partially reserved by Cur treatment (Fig. 5G and H).

To facilitate a better comparison of species abundance differences between different groups, we constructed a heatmap of intergroup differential species, allowing for a more convenient observation of the variations in species abundance across groups. The analysis was based on the top 30 species in terms of abundance; if fewer than 30 species were detected, all detected species were displayed. Heatmaps showing the differences in species at the genus and species levels between groups are presented in (Fig. 5I and J). To further distinguish the species that differ significantly between the groups, we conducted LEFSe analysis. A total of 72 taxa were identified from phylum to genus level, comprising 12 taxa in the control group, 50 taxa in the model group, and 10 taxa in the Cur group. The taxa with the most significant differences in abundance were *Limosilactobacillus_vaginalis*_A and *Bacteroides*_sp002491635 for the Cur group, *Bacteroidaceae*, *Verrucomicrobiales*, *Verrucomicrobiae* and *Akkermanceae* for the model group, *Ileibacterium_valens* and *Prevotella_rara* for the control group (Fig. 5K).

3.6. Cur orchestrates serum metabolite profiles in CRC mice

In a bid to discern potential metabolites and pathways elicited by Cur, an untargeted metabolomic examination of serum was

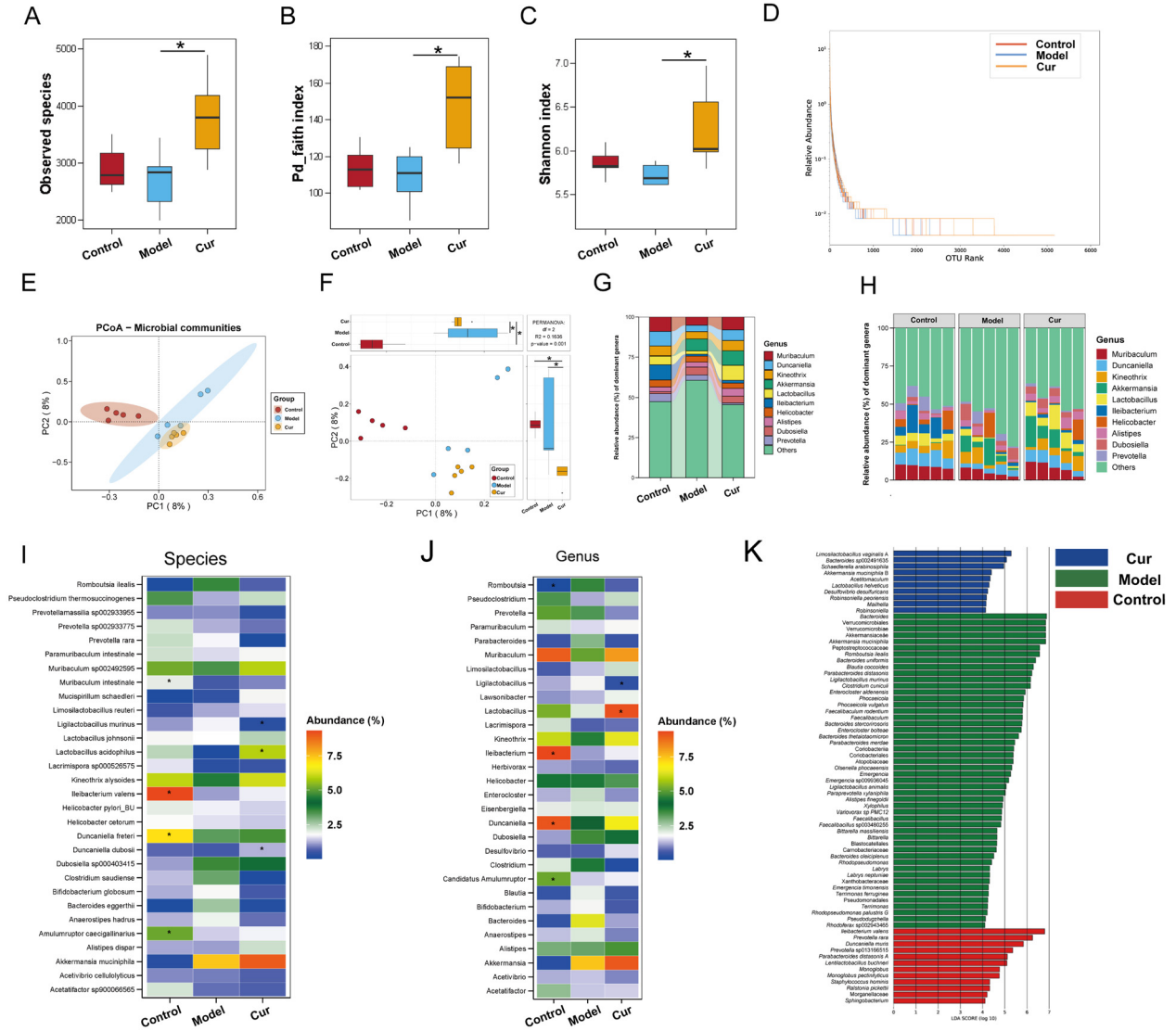

Fig. 5 Cur modulated the gut microbiome composition (A, B and C) alpha diversity of the gut microbiome. (D) Rank abundance curves. (E and F) PCoA in different groups. (G and H) Alluvial chart of the differential species abundance at the genus level. Heatmap of intergroup differences at the (I) species and (J) genus levels. (K) LEfSe analysis (n = 5). *p < 0.05 *vs* model group.

undertaken utilizing LC-MS. The ensuing OPLS-DA analysis delineated a pronounced differentiation in metabolic profiles across the 3 taxa, alongside a notable reproducibility of samples within each taxon. In accordance with the results derived from random permutation tests conducted on the OPLS-DA model, the R2 values were observed to be 0.834, 0.887, and 0.968, respectively, each surpassing the threshold of 0.5. Concurrently, the Q2 values were noted to be negative, which collectively suggests that the established OPLS-DA model exhibits a robust and reliable statistical framework (Fig. 6A). In the comparison between the model group and the control group, a total of 940 differential metabolites were identified, with 471 being downregulated and 469 upregulated. Conversely, the comparison between the Cur group and the model group revealed 801 differential metabolites, consisting of 385 downregulated and 416 upregulated species (Fig. 6B). To provide a more visually intuitive representation of the categorization of metabolites, we have employed pie charts to delineate the distribution across various hierarchical levels, namely Class, Super Class, and Sub Class (Fig. 6C). Given the extensive range of categories, we have selectively focused on the nine most populous categories of metabolites, while aggregating the remaining categories under the designation of 'others'. The pie chart illustrating the distribution within the Class categorization is presented in the subsequent figure. Within the hierarchical classification scheme encompassing Class, Super Class, and Sub Class, the predominant categories are as follows: 'Fatty Acyls' represents the most abundant group within the 'Class' level, 'Amino Acid, Peptides, and Analogues' dominates the 'Super Class' category, and 'Lipids and Lipid-

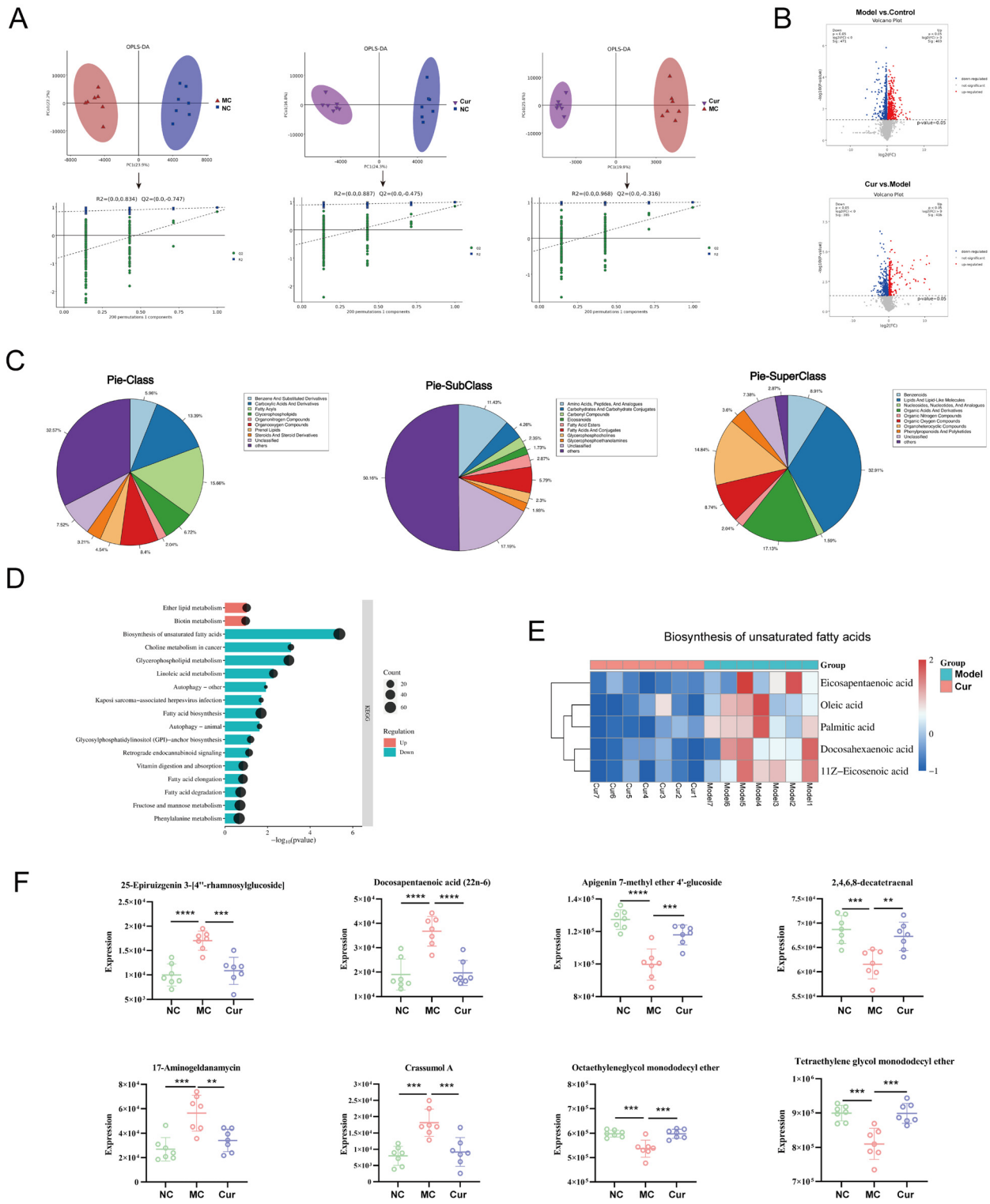

Fig. 6 (A) The OPLS-DA score plots distribution and permutation test charts for the OPLS-DA model. (B) Volcano map of serum metabolites. (C) The metabolites are categorized according to class, Super-class, and Subclass. (D) KEGG differential pathway enrichment bubble diagram between model group and Cur group. (E) Metabolites associated with Biosynthesis of UFAs. Bar Chart of Selected Differential Metabolites (n = 7). (F) Key differential metabolites regulated by Cur (n = 7). *p < 0.05; **p < 0.01; ***p < 0.001; ****p < 0.0001 *vs.* model group.

Like Molecules' emerges as the leading class within the 'Sub Class' tier. Pathway enrichment analysis was conducted using the KEGG IDs of differential metabolites between the Cur group and model group, yielding results in metabolic pathway enrichment. Enrichment was primarily observed in pathways such as the Biosynthesis of UFAs, Glycerophospholipid (GPL) Metabolism, Biotin Metabolism, and Choline Metabolism in Cancer (Fig. 6D). Subsequently, we generated heatmaps for metabolites enriched in significantly different pathways to observe the specific upregulation and downregulation of metabolites within these pathways. In the Biosynthesis of UFAs, a post-treatment downregulation was observed for Eicosapentaenoic acid, Oleic acid, Palmitic acid, Docosahexaenoic acid, and 11*Z*-Eicosenoic acid (Fig. 6E). Subsequently, we discovered that Cur can modulate the disrupted serum metabolism in CRC mice, restoring some of the metabolites to normal levels (Fig. 6F).

3.7. Correlation analysis between gut microbiota and differential metabolites

In this study, we investigated the correlation between gut microbiota and metabolites by exploring interactions between microbial genera and metabolites through correlation analysis. The results showed that *Lactobacillus* was significantly positively correlated with 13 metabolites, especially with Punicic acid, PC (16:0120:3(6,8,11)-0H (5)), Hexadecenal, and others. This suggests that *Lactobacillus* may significantly impact host metabolism by metabolizing metabolites such as Punicic acid. *Duncaniella* exhibited a positive correlation with D-Mannose, contrasting with *Romboutsia*, highlighting the complex relationship between gut microbiota and metabolism. Additionally, *Parabacteroides* and *Romboutsia* displayed a close relationship with metabolites. Sixteen metabolites were negatively correlated with *Romboutsia*, and five metabolites were positively correlated with it. Ten metabolites were negatively correlated with both *Romboutsia* and *Parabacteroides*, and five metabolites were positively correlated (Fig. 7). These findings help us understand how gut microbiota influences host health through metabolites and provide new clues for future exploration of its relationship with diseases like metabolic syndrome.

3.8. FMT inhibits tumor growth and enhances $CD8^+$ T cell-mediated antitumor immunity

To assess whether gut microbiota contributes to the antitumor effect of Cur and $CD8^+$ T cell infiltration, we conducted FMT experiments. We found that C-FMT inhibited tumor growth,

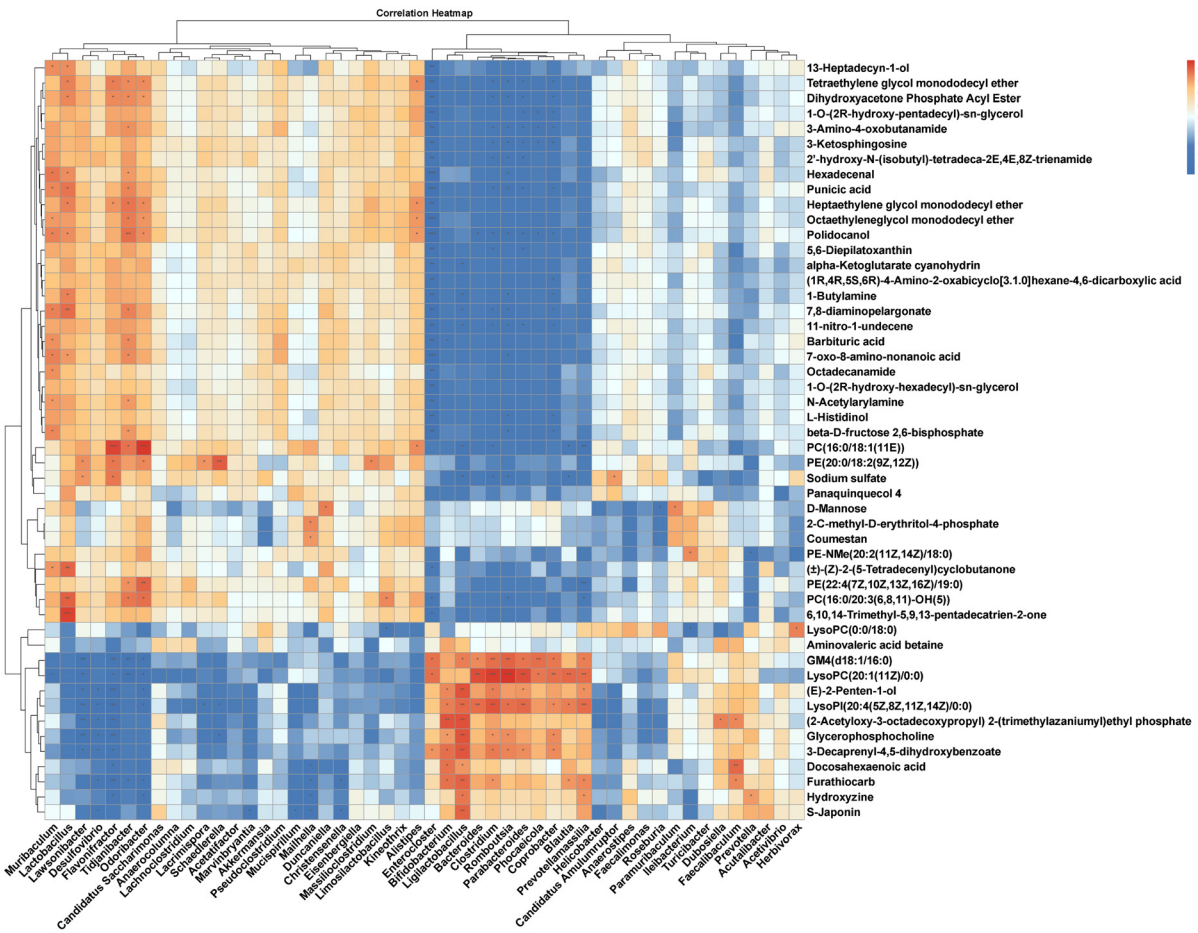

Fig. 7 Correlation analysis between key genera and metabolites with significant changes. *$p < 0.05$; **$p < 0.01$; ***$p < 0.001$.

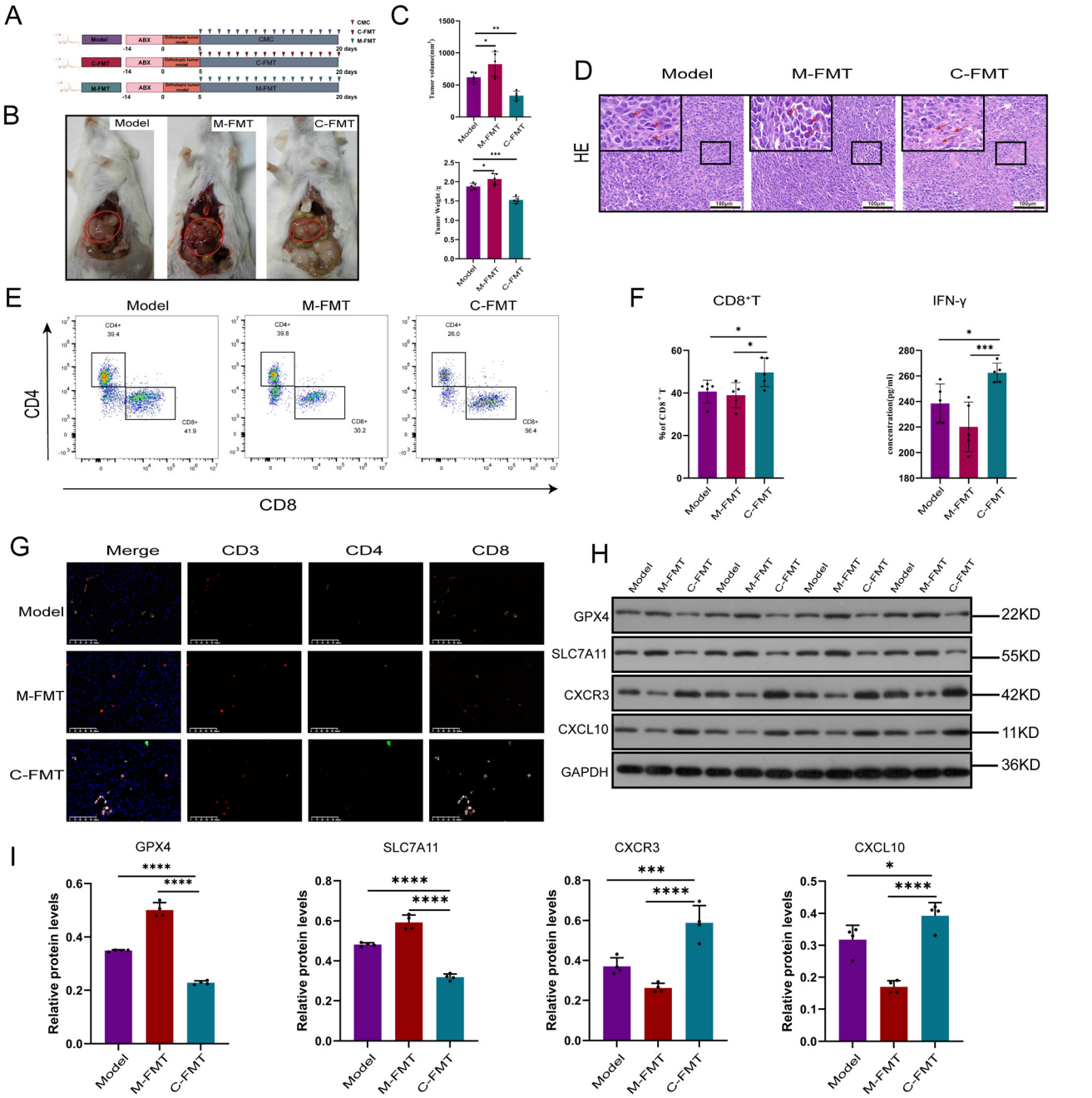

Fig. 8 The Cur-treated FMT increased CD8$^+$ T Cell tumor infiltration and ferroptosis. (A) Experimental procedure of FMT (B and C) Tumor volume and weight. (D) H&E of tumor tissues. Scale bar = 100 μm. (E) The expression of CD8$^+$ T cells was determined by flow cytometry analysis. (F) CD8$^+$ T and IFN-γ statistical analysis bar chart. (G) Representative immunofluorescent staining of CD3$^+$, CD4$^+$, and CD8$^+$ T cells in tumor tissues. Scale bar = 50 μm. (H and I) The expression of GPX4, SLC7A11, CXCR3, and CXCL10 protein in tumor tissues (n = 5). *p < 0.05; **p < 0.01; ***p < 0.001; ****p < 0.0001 *vs* model group.

whereas M-FMT accelerated it (Fig. 8A and B). H&E staining revealed increased necrotic foci in tumor tissues following C-FMT (Fig. 8C). Triple-labeling immunofluorescence showed that C-FMT increased the expression of CD3-positive (pink), CD4-positive (green), and CD8-positive (red) cells in tumor tissues (Fig. 8F). We further confirmed a significant increase in CD8$^+$ T cell infiltration in tumor tissues using flow cytometry (Fig. 8D). To further examine the effect of FMT on CD8$^+$ T cell function, we measured cytokine secretion *via* ELISA, and found that IFN-γ secretion was significantly increased after C-FMT, consistent with previous experiments (Fig. 8E). CXCL10-CXCR3 signaling is crucial for T cell tumor infiltration and immunotherapy. The transcriptional expression of CXCR3 ligands correlates with CD8$^+$ T cell infiltration and prolonged

survival in CRC, with CXCL10 identified as a ligand for CXCR3. To elucidate the mechanism by which FMT enhances $CD8^+$ T cell infiltration into tumors, we used WB to detect changes in the CXCR3/CXCL10 axis. We found that C-FMT increased the expression of CXCR3 and CXCL10 proteins (Fig. 8G and H). Moreover, C-FMT induced ferroptosis, evidenced by the reduced expression of GPX4 and SLC7A11 proteins (Fig. 8G and H).

3.9. Cur inhibits tumor growth and enhances antitumor immunity in a gut microbiota dependent manner

To investigate whether the gut microbiota is involved in the inhibitory effect of Cur on CRC and the recruitment of $CD8^+$ T cells, the gut microbiota of mice was depleted before establishing the CRC model. As shown in (ESI Fig. S2†), the mice were first treated with antibiotics *via* oral gavage for 14 days, and then Cur was administered by gavage after successful tumor modeling. Surprisingly, after gut microbiota depletion, there were no differences in tumor volume (ESI Fig. S2B†) histopathological staining (ESI Fig. S2C†), or $CD8^+$ T cell infiltration levels (ESI Fig. S2D and E†) between the ABX + CMC group and the ABX + Cur group mice. These results indicate that the inhibitory effect of Cur on CRC and the recruitment of $CD8^+$ T cells depend on the gut microbiota.

4. Discussion

CRC has witnessed significant therapeutic advancements in recent years, yet it confronts several pivotal challenges. The efficacy of immunotherapy in CRC is impeded by individual variability and low response rates, particularly in tumors categorized as immunologically 'cold'.[37] Chemotherapy dosing, traditionally based on body surface area (BSA), often results in suboptimal drug concentrations, heightening the risk of adverse reactions.[38] Addressing these challenges is imperative for enhancing therapeutic efficacy and patient survival outcomes in CRC. Cancer management is increasingly recognizing the importance of dietary phytochemicals in prevention and treatment. These natural compounds, found in a variety of fruits, vegetables, and plants, have been researched for their beneficial effects against cancer. Phytochemicals function through multiple mechanisms, including antioxidation, and anti-inflammation, regulating cell proliferation and apoptosis, and affecting the metabolism of cancer cells. Consequently, the incorporation of these compounds into daily diet is being considered more prominently in the comprehensive management strategies for cancer. Melatonin, recognized for its presence in various plants, exerts anti-CRC effects through modulation of key pathways including COX-2, TNF-α, and iNOS. This compound's influence extends to the PI3K/Akt and nuclear factor NF-κB pathways, contributing to its efficacy in preclinical models.[39] Additionally, ginsenosides, derived from ginseng, have been identified as potent modulators of the TME and immune cell functionality, further impeding tumor growth and metastasis while altering cancer cell metabolism.[40] Cur is found to regulate the gut microbiota, thereby influencing the pathogenesis of CRC.[41] It helps restore the balance of the gut microenvironment by inhibiting the growth of harmful bacteria and promoting beneficial ones, which is crucial in preventing intestinal inflammation and tumor development.[42] Furthermore, Cur can influence the metabolic products of the gut microbiota, such as short-chain fatty acids, thereby affecting intestinal immune responses and cancer cell metabolism.[43] Turmeric and Cur are non-mutagenic and non-genotoxic. At certain doses, oral administration of turmeric and Cur does not cause reproductive toxicity in animals. Studies in humans have shown that Cur is safe when taken orally at a dose of 6 grams per day for 4–7 weeks, although some gastrointestinal discomfort may occur. Oral formulations of Cur at a dose of 500 mg twice daily for 30 days are also considered safe for humans, though nano-formulations require further research. Overall, turmeric and Cur are regarded as safe, particularly for oral use.[44] Although current research findings are encouraging, more clinical studies are needed to further elucidate the specific mechanisms and long-term effects of Cur in modulating the gut microbiota for CRC treatment. In this study, we investigated the anti-cancer effects of Cur on CRC. Our findings revealed that Cur significantly inhibited tumor growth in CRC mouse model, underscoring its potential as an anti-tumor agent. Further evaluation highlighted Cur's modulatory on the TIME, notably by enhancing $CD8^+$ T cell tumor infiltration. Additionally, it was found that Cur can induce ferroptosis in CRC mice by inhibiting the SLC7A11/GPX4 signaling pathway. To elucidate the underlying mechanisms, we conducted 16S sequencing and metabolomic analysis, providing evidence for exploring the anti-tumor mechanisms of Cur.

In the dynamic TME of CRC, $CD8^+$ T cells are pivotal in mediating tumor eradication and immune regulation. Recent research has shed light on the intricate interplay between $CD8^+$ T cells and the TME, underscoring their cytotoxic potential and the TME's role in suppressing immune function. For instance, cancer cells orchestrate a glucose-deprived, lactate-rich TME, impairing $CD8^+$ TILs while promoting Treg cell-mediated immune suppression. Targeting this metabolic competition enhances $CD8^+$ T cell activation and cytotoxicity, as evidenced by interventions disrupting aerobic glycolysis in cancer cells, thereby destabilizing Treg cells and fostering a conducive environment for $CD8^+$ TILs.[45] Ferroptosis is a new type of iron-dependent programmed cell death, which is different from other types of cell death. Since its discovery as an iron-dependent form of non-apoptotic cell death in 2012, ferroptosis has gained increasing attention in cancer research, offering the potential for its application in cancer therapeutics.[46] It's primarily characterized by lipid peroxidation and impaired activity of GPX4. Inadequate GPX4 functionality exacerbates lipid peroxidation, leading to increased cellular vulnerability. Within the oncological paradigm, ferroptosis represents a promising avenue for targeting chemo-resistant tumor cells, circumventing conventional apoptotic resistance pathways. Recent advancements in the field have demonstrated the augmentation of cancer therapeutic efficacy

through the modulation of ferroptotic pathways, either by inhibiting GPX4 activity or enhancing intracellular iron concentrations.[47,48] Additionally, manipulating iron metabolism within the tumor microenvironment or utilizing ferroptosis inducers has emerged as a viable anti-cancer strategy.[49] This study demonstrated that Cur significantly inhibited tumor growth in CRC mouse models. This effect is likely attributed to an increase in the number of $CD8^+$ T cells within the tumor, coupled with restoration of their normal antitumor immune functions. This restoration was evident at the cytokine secretion level, as observed through enhanced levels of IL-2, TNF-α, and IFN-γ, quantified *via* ELISA. Oxaliplatin primarily induces cell death in rapidly dividing cells by inhibiting DNA synthesis. However, recent studies have shown that oxaliplatin can also modulate the immune microenvironment, including increasing $CD8^+$ T cell infiltration, which contributes to its antitumor effects. This mechanism may be related to immunogenic cell death (ICD). Reports indicate that oxaliplatin can induce ICD, a process that releases danger signals and subsequently enhances the antitumor immune response.[50] Additionally, we quantify changes in the concentrations of Iron, SOD, MDA, and GSH within the tumor tissues. Our observations indicated a significant decrease in the levels of SOD and GSH post-treatment, particularly in the oxaliplatin group and Cur-H group. Conversely, there was a marked increase in the level of Iron and MDA in the tumor tissues following treatment. In the subsequent phase, we utilized WB analysis to investigate changes in proteins associated with ferroptosis. This analysis revealed that Cur effectively reduced the expression of GPX4 and SLC7A11 proteins. These findings suggest a potential mechanism by which Cur exerts its antitumor effects, highlighting its role in modulating the immune response against CRC.

Gut microbiota dysbiosis is considered a key factor in CRC development. Studies have identified differences in gut microbiota composition between individuals with CRC and healthy individuals, including disparities in fecal bacterial diversity.[51] CRC alters the abundance and diversity of the gut microbiota, a condition partially mitigated by Cur. Clinical studies have found that the genus *Parabacteroides* is significantly enriched in the feces of stage III–IV CRC patients, indicating its potential as a microbial biomarker for CRC staging.[52] Research on the gut microbiota as a CRC biomarker has advanced in recent years; studies show that the microbiota, including *Romboutsia*, can distinguish CRC patients from healthy individuals.[53] An investigation into gut microbiota characteristics in an early CRC animal model found that the abundance of *Romboutsia* was higher in CRC rats than in normal rats, providing insights into the role of gut symbionts in CRC progression.[54] These findings suggest that changes in gut microbiota offer potential biomarkers for CRC staging and early diagnosis, and lay the foundation for understanding CRC pathogenesis and exploring new therapeutic strategies. In our study, we observed an increased abundance of gut symbionts like *Romboutsia* and *Parabacteroides* in the Model group, further implicating these genera in CRC progression. In CRC mice treated with Cur, the abundance of *Romboutsia* and *Parabacteroides* was reduced, indicating that Cur may exert its anti-CRC effects by modulating these genera. Chronic intestinal inflammation can cause cellular damage, DNA mutations, and changes in the immune microenvironment, promoting abnormal proliferation and carcinogenesis of intestinal epithelial cells. A study in DSS-induced colitis mice found that a microbial member of *Duncaniella*, NHRI-C1-K-H-1-87, protected the host from DSS-induced injury, modulated the gut microbiota, and counteracted DSS-induced dysbiosis, highlighting its potential as a next-generation probiotic for colitis.[55] The gut microbiota promotes CRC development through its microbes and metabolites. A study investigating gut microbiota composition at different stages of CRC and the effects of FMT on CRC mice found that mice receiving fecal microbiota from healthy volunteers had a higher abundance of *Ileibacterium* than those receiving microbiota from IBD, CRC, or CRA patients. This underscores the beneficial role of *Ileibacterium* in gut health and cancer prevention, with FMT from healthy volunteers suppressing CRC progression in mice, while FMT from CRC patients exacerbated the disease.[56] Our study similarly found that the abundance of *Duncaniella* and *Ileibacterium* in the model group was significantly lower than in healthy mice, with their levels partially restored after Cur treatment. These studies suggest that restoring a healthy gut microbiota may help control CRC progression. *Lactobacillaceae* microorganisms play a crucial role in CRC progression. These microbes influence CRC prevention and treatment by modulating the gut environment, enhancing intestinal barrier function, and immune response. *Lactobacilli* produce anti-inflammatory and anticancer compounds, such as SCFAs, which are key in suppressing intestinal inflammation and carcinogenesis.[57] Some *Lactobacillus* strains directly affect the growth and apoptosis of cancer cells.[58] The abundance of *Lactobacillus* was significantly higher in the Cur group compared to the Model group. *Lactobacillus*, a genus of lactic acid bacteria, plays a significant role in the pathogenesis and progression of CRC. Notably, *L. acidophilus* KLDS1.0901 has demonstrated anti-proliferative effects on human CRC cell lines, revealing its potential to directly inhibit tumor cell growth.[59] *L. gallinarum* contributes to the prevention of intestinal tumor formation by generating protective metabolites that induce apoptosis in CRC cells.[60] We also observed changes in the abundance of *Kineothrix*. Compared with the Control group, the abundance of *Kineothrix* was lower in the Model group, while its abundance was partially restored in the Cur group. *Kineothrix* is associated with SCFA production and the regulation of gut microbiota composition, which may support intestinal health and metabolic stability.[61,62] Cur can increase the abundance of SCFA-producing microbes in the gut, such as *Lactobacillus* and *Kineothrix*. We speculate that this may be one of the mechanisms by which Cur exerts its anti-CRC effects; however, our study lacks further experimental validation. In conclusion, these findings suggest that Cur holds significant potential in preventing and treating CRC. It is worth noting that due to the poor water solubility of Cur, a solubilizing agent was required

to facilitate its dissolution/suspension for intragastric administration in this study. Based on our disease model, we selected CMC-Na to prepare the Cur suspension. The key advantage of CMC-Na lies in its ability to prolong the retention time of the drug in the intestinal tumor site after intragastric administration, thereby enhancing therapeutic efficacy. Additionally, this carrier exhibits extremely low toxicity in animals and forms a uniform suspension system. However, previous studies have shown that CMC-Na possesses prebiotic/microbiome-modulating properties, as it has been reported to promote the growth of *Akkermansia muciniphila* and modulate bioreactor intestinal models.[63] We have controlled for this factor in our study by using a low concentration of 1% CMC-Na (corresponding to a daily intake of $<0.2\ g\ kg^{-1}$), which is far below the threshold (>5%) typically required to produce significant prebiotic effects. Nevertheless, dietary microbiome changes induced by Cur may, to some extent, interact synergistically with CMC-Na or even involve bacterial cross-feeding, making the process more complex.

Recent advances in metabolomics have enhanced our understanding of CRC mechanisms, particularly within the TME. Our metabolomic analysis revealed that serum metabolites, including Docosapentaenoic acid (22n-6), 17-Aminogeldanamycin, Apigenin 7-methyl ether 4′-glucoside, 2,4,6,8-decatetraenal, and Crassumol, are closely linked to CRC pathogenesis. A Mendelian randomization study found that genetically predicted higher Docosapentaenoic acid levels are positively associated with lung cancer, with a 1% increase corresponding to a 2.01-fold higher risk.[64] This trend aligns with our findings: mice in the Model group exhibited elevated serum levels of Docosapentaenoic acid, which were restored to Control group levels after Cur treatment. Studies in melanoma have shown that 17-Aminogeldanamycin alleviates the compensatory rise in HSP70 mRNA and induces endoplasmic reticulum stress, leading to a selective reduction in IRE1α-XBP1s pathway activity, ERK1/2 inhibition, and apoptosis.[65] Furthermore, 17-Aminogeldanamycin inhibits NF-κB activity and reduces IL-8 and VEGF levels in the melanoma extracellular environment.[66] In contrast, our study observed an increase in serum 17-Aminogeldanamycin levels in CRC mice, which declined after Cur treatment. Although the precise role of 17-Aminogeldanamycin in CRC remains unclear, its contrasting behavior across tumor types has captured our attention, offering new avenues for future research. These metabolites could serve as CRC biomarkers, offering insights into its molecular basis and aiding early detection and targeted therapy development. UFAs play a dual role in tumor development. Studies indicate that UFAs promote tumorigenesis by enhancing the immunosuppressive TME through FABP5-PPARγ signaling.[67] UFAs are also positively correlated with SCD1/FADS2 levels and the oncogenic potential of OvCa cells.[68] A population-based cohort study from the UK Biobank found that higher plasma levels of omega-6 and omega-3 fatty acids—types of polyunsaturated fatty acids—are associated with a reduced overall cancer risk.[69] Our study found that the UFA biosynthesis pathway was significantly enriched after treatment, and associated metabolites, including Eicosapentaenoic acid, Oleic acid, Docosahexaenoic acid, and 11Z-Eicosenoic acid, declined, suggesting that Cur may exert its anti-CRC effects by inhibiting UFA biosynthesis. The GPL and biotin metabolism pathways play critical roles in CRC progression. During cancer progression, tumor cells undergo metabolic reprogramming to support rapid growth, including changes in biotin-dependent pathways. Increased fatty acid synthesis—a hallmark of many cancers—is critically dependent on biotin. Changes in the gene expression of enzymes involved in biotin metabolism have been observed in some cancers, potentially impacting tumor cell growth and survival. Variations in biotin levels can influence the TME by affecting immune cell function and interactions between tumor cells and surrounding tissues. Recent CRC studies highlight the significant role of biotin metabolism. A pivotal study revealed a marked decrease in biotin content in colorectal adenocarcinoma cells compared to normal mucosa. This finding correlates with the downregulation of the PCCA and PCCB genes, integral to propionyl-CoA carboxylase (PCC) activity, a biotin-dependent enzyme.[70] This suggests a potential link between reduced biotin levels and metabolic alterations in CRC. These findings suggest that Cur may hold significant potential in the prevention and treatment of CRC.

Metabolites derived from the gut microbiota serve as key intermediaries linking the microbiome to cancer progression, mainly by remodeling the TME and regulating key signaling pathways in tumor and immune cells. To investigate the correlation, we cross-validated differential metabolites and microbial community changes at the genus level. In the 16S sequencing, we observed changes in the abundance of genera such as *Parabacteroides*, *Romboutsia*, *Duncaniella*, *Ileibacterium*, *Lactobacillus*, and *Kineothrix*. However, the relationships between these genera and related metabolites, and their impact on CRC progression, remain unclear. We then performed a Pearson correlation analysis. The results showed that *Lactobacillus* was positively correlated with metabolites such as PC (16:0120:3(6,8,11)-0H (5)), Hexadecenal, and Punicic acid. This suggests that increased *Lactobacillus* abundance may exert an anti-CRC effect by modulating these metabolic pathways. Studies have shown that Punicic acid is highly cytotoxic to HCT-116 colorectal and FaDu hypopharyngeal carcinoma cells, both in monolayer and 3D spheroid cultures. Punicic acid also triggers ferroptosis in carcinoma cells, inducing significant lipid peroxidation, which can be mitigated by ferroptosis inhibitors.[71] We observed ferroptosis in tumor cells in this study, where $CD8^+$ T cells secrete IFN-γ, downregulating SLC7A11 and inhibiting ferroptosis. The ferroptosis process mediated by *Lactobacillus* and Punicic acid metabolism is significant in tumor cell progression. Its anti-tumor effects have been observed in glioblastoma and breast cancer cells, potentially through the PI3K/AKT1/mTOR signaling pathway.[72,73] In addition, increased *Duncaniella* abundance was positively correlated with D-Mannose levels. Research has shown that D-Mannose targets PD-L1 degradation, significantly enhancing the treatment of triple-negative breast cancer. Specifically,

D-Mannose activates AMP-activated protein kinase, phosphorylating PD-L1 at the S195 site, leading to abnormal glycosylation and proteasomal degradation of PD-L1, promoting T cell activation and T cell-mediated tumor cell killing.[74] Although this phenomenon has not been observed in CRC, it offers valuable insights. Our study observed increased $CD8^+$ T cell infiltration and enhanced secretion of immune factors in tumor tissues. We previously observed that the abundance of *Romboutsia* and *Parabacteroides* increased in the model group and returned to normal levels after Cur treatment, highlighting their potential as diagnostic markers in CRC. In the correlation analysis, we found that *Romboutsia* and *Parabacteroides* were negatively correlated with Punicic acid, further supporting their role in CRC progression. These findings indicate that metabolites derived from the gut microbiota may serve as potential biomarkers for CRC, offering insights into its molecular basis and supporting early detection and targeted therapy development.

Previous studies have established that the gut microbiota modulates the host's antitumor immune response and exhibits relevance to cancer immunotherapy.[75] It has been observed in germ-free mice that immunotherapies lose their efficacy, which can be restored through FMT or supplementation with specific bacterial strains.[76,77] Metabolites produced by gut microbiota have also been demonstrated to influence the development and progression of CRC. For instance, the concentration of butyrate shows an inverse correlation with CRC incidence. Butyrate produced by Roseburia intestinalis has been shown to enhance anti-PD-1 therapy in CRC by activating $CD8^+$ cytotoxic cells.[78] Building on these insights, our study investigated the regulatory effects of Cur on gut microbiota and $CD8^+$ T cells. We conducted FMT experiments to determine whether the modulation of $CD8^+$ cells by Cur could be transferred through FMT. Our findings revealed that FMT from mice in the Cur group markedly inhibited tumor growth and increased $CD8^+$ T cell infiltration in tumor tissues. Conversely, FMT from mice in the model group exacerbated disease progression, as evidenced by accelerated tumor growth and reduced infiltration of $CD8^+$ T cells in the tumor tissues. Additionally, when gut microbiota was depleted with antibiotics, Cur's antitumor effects disappeared, suggesting that Cur mitigates CRC in a gut microbiota-dependent manner. Tumor infiltration of $CD8^+$ T cells is regulated by multiple factors, among which the CXCR3/CXCL10 axis represents a pivotal pathway. CXCR3, a chemokine receptor abundantly expressed on $CD4^+$ T cells, $CD8^+$ T cells, and NK cells, binds to its ligand CXCL10.[79] This interaction not only recruits $CD4^+$ and $CD8^+$ effector T cells to the tumor site but also guides their polarization and enhances their biological functions.[80,81] In this study, FMT from the Cur group of mice not only enhanced $CD8^+$ T cell infiltration in tumor tissues but also demonstrated activation of the CXCR3/CXCL10 axis. Conversely, FMT from the model mice exhibited an opposite trend. Interestingly, $CD8^+$ T cells can regulate tumor ferroptosis during cancer immunotherapy. $CD8^+$ T cells have been found to regulate tumor ferroptosis during cancer immunotherapy. The IFN-γ secreted by $CD8^+$ T cells downregulate SLC7A11, inhibiting cystine uptake in tumor cells, thereby promoting lipid peroxidation and ferroptosis in these cells.[82] This may underlie the mechanism by which Cur induces ferroptosis in tumor cells in this study.

Due to its tolerance to low pH levels, Cur remains highly stable in gastric acid. After oral administration, Cur is scarcely absorbed in the stomach, but high concentrations can be detected in the gastrointestinal tract. Without any chemical modifications, Cur reaches the colon and undergoes extensive phase I and phase II metabolism, generating active metabolites such as dihydrocurcumin, tetrahydrocurcumin, and hexahydrocurcumin.[83–85] Concentrations in plasma and urine are very low after oral administration, which may be due to the fact that Cur derivatives are not always measured, thus underestimating its absorption. As previously noted, Cur mainly exerts its regulatory effects in the intestine, where high concentrations are present after oral administration.[86] Therefore, Cur may have the potential to directly regulate intestinal barrier function and modulate impaired signaling pathways. Additionally, it may act at the intestinal level by promoting changes in the composition and diversity of the gut microbiota.[87] In HPLC analysis of Cur bioavailability in rats, significant differences were observed in its distribution, with Cur concentrations being notably higher in the intestine compared to other tissues and serum. In contrast, Cur levels in the serum, liver, and fat were similar, while its concentration in the intestinal reached 482 ng g^{-1} tissue.[86] A study conducted on healthy adult volunteers involved consuming a standardized dose of dried Cur extract for 28 days, followed by metabolomic analysis of 24 h urine samples to better understand changes in metabolite composition. The results revealed that Cur induced changes in urinary metabolites, particularly those related to fatty acid metabolism, energy production, and inflammation-related compounds, suggesting a crucial role for Cur in regulating metabolic and anti-inflammatory pathways. Moreover, changes in several microbial metabolites clearly demonstrated Cur's intestinal absorption and the metabolic activity of the gut microbiota, further proving the interaction between Cur and the gut microbiota.[87] The potential role of the gut microbiota in mediating Cur's bioactivity represents an intriguing and attractive research direction. As highlighted by the considerable attention given to the stark contrast between the potent biological effects of certain functional foods and their low bioavailability, this aligns with our findings: Cur, despite its low bioavailability, was able to exert significant anti-CRC effects, which disappeared when the gut microbiota was depleted by antibiotics, clearly indicating the relationship between Cur's activity and the gut microbiota. For oral drugs and functional foods, bioavailability is traditionally defined as "the amount or proportion of the ingested dose that is directly absorbed into circulation through the small intestine". However, since the gut microbiota is effectively considered an active bioreactor in the human gut and given the emerging interactions between functional foods and the gut microbiota, it might be time to redefine the concept of bioavailability.

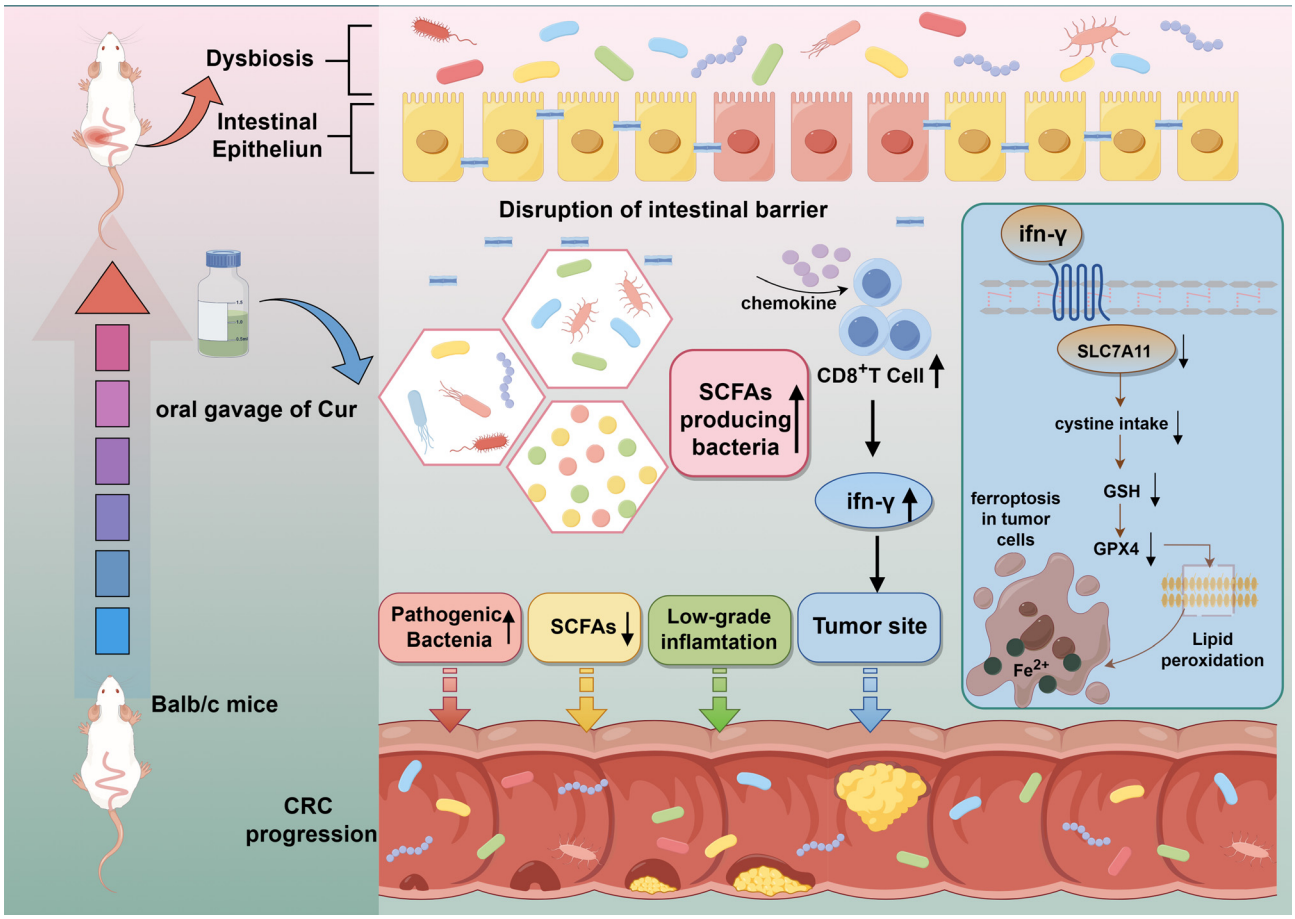

Fig. 9 Diagram of the underlying mechanism of Cur in CRC treatment.

5. Conclusions

This study highlights the significant anti-tumor effects of Cur, likely due to its role in promoting $CD8^+$ T cell infiltration into tumor tissues. The increase in the quantity and functional restoration of $CD8^+$ T cells enhances their cytotoxicity, with $CD8^+$ T cell infiltration and IFN-γ secretion identified as key inducers of ferroptosis in tumor cells. Cur also regulates the abundance of probiotics and SCFA-producing microbes, with its anti-CRC and immune-modulatory effects transferable *via* FMT. From a metabolomic perspective, Cur exerts its effects by modulating pathways such as GPL metabolism, UFA biosynthesis, and biotin metabolism. Additionally, the correlation analysis revealed a close relationship between changes in gut microbiota abundance and metabolites. The abundance changes in genera like *Lactobacillus* and *Kineothrix*, which have potential anti-cancer and immune-modulatory roles, show spatiotemporal consistency with metabolites such as Punicic acid and D-Mannose, key in CRC occurrence and development, including inducing ferroptosis in tumor cells. However, when the gut microbiota was depleted using antibiotics, the anti-tumor effects of Cur were lost, further validating the role of the gut microbiota in Cur-induced $CD8^+$ T cell recruitment. This study provides new insights into CRC mechanisms and proposes new therapeutic interventions, highlighting the interaction between gut microbiota and immune responses in the tumor immune microenvironment. This suggests that its immune-modulatory effects may be mediated through gut microbiota and their metabolic pathways (Fig. 9).

However, several limitations remain in this study. For instance, FMT was administered repeatedly throughout the experiment but was not used to initially establish a control or cur-microbiome in the recipient mice, as the recipient's microbiome was not confirmed to match the donor's. Additionally, our study employed only 16S rRNA gene sequencing, which provides insights into microbial composition but does not directly reveal functional gene content. Metagenomic analysis of the microbiome would have been more effective in linking the observed functional metabolic changes, such as phospholipid metabolism, UFA biosynthesis, and biotin metabolism, to specific microbial pathways. Understanding the pharmacokinetics of Cur, particularly its plasma concentration, is crucial to determining whether its anti-tumor effects are primarily mediated by immune activation or direct cytotoxicity, which is key for evaluating the translational potential of curcumin-based therapies. Due to resource and time limitations, phar-

macokinetic analyses to measure plasma curcumin concentrations were not conducted. We acknowledge this limitation, which restricts a full understanding of Cur's mechanisms of action. We will conduct relevant experiments in future studies to improve our research.

Author contributions

Hongli Zhou: investigation, visualization, methodology, and writing – original draft. Yupei Zhuang: investigation and methodology. Yuwei Liang: investigation. Haibin Chen: investigation. Wenli Qiu: writing – review & editing. Hongguang Zhou: conceptualization, funding acquisition, supervision, and writing – review & editing. Huiqin Xu: project administration, supervision, and writing – review & editing.

Data availability

The data supporting this article have been included as part of the ESI.†

Conflicts of interest

The authors declare no conflict of interest.

Acknowledgements

This research was funded by the National Natural Science Foundation of China, grant number "82001883, 81973737" and a project funded by the Graduate Student Research Innovation Program of Jiangsu Province, grant number "KYCX23_2045". We thank Figdraw (**http://www.figdraw.com**) for their help in creating the Mechanism diagram.

References

1 R. L. Siegel, N. S. Wagle, A. Cercek, R. A. Smith and A. Jemal, Colorectal cancer statistics, 2023, *CA A Cancer J. Clinicians*, 2023, **73**(3), 233–254.
2 R. Sharma, M. Abbasi-Kangevari and R. Abd-Rabu, Global, regional, and national burden of colorectal cancer and its risk factors, 1990–2019: a systematic analysis for the Global Burden of Disease Study 2019, *Lancet Gastroenterol. Hepatol.*, 2022, **7**(7), 627–647.
3 E. F. Onyoh, W.-F. Hsu, L.-C. Chang, Y.-C. Lee, M.-S. Wu and H.-M. Chiu, The Rise of Colorectal Cancer in Asia: Epidemiology, Screening, and Management, *Curr. Gastroenterol. Rep.*, 2019, **21**(8), 36.
4 T. Sawicki, M. Ruszkowska, A. Danielewicz, E. Niedźwiedzka, T. Arłukowicz and K. E. Przybyłowicz, A Review of Colorectal Cancer in Terms of Epidemiology, Risk Factors, Development, Symptoms and Diagnosis, *Cancers*, 2021, **13**(9), 2025.
5 M. Schmitt and F. R. Greten, The inflammatory pathogenesis of colorectal cancer, *Nat. Rev. Immunol.*, 2021, **21**(10), 653–667.
6 S. Man, J. Yao, P. Lv, Y. Liu, L. Yang and L. Ma, Curcumin-enhanced antitumor effects of sorafenib *via* regulating the metabolism and tumor microenvironment, *Food Funct.*, 2020, **11**(7), 6422–6432.
7 X.-C. Zhao, L. Zhang, H.-X. Yu, *et al.*, Curcumin protects mouse neuroblastoma Neuro-2A cells against hydrogen-peroxide-induced oxidative stress, *Food Chem.*, 2011, **129**(2), 387–394.
8 K. Burge, A. Gunasekaran, J. Eckert and H. Chaaban, Curcumin and Intestinal Inflammatory Diseases: Molecular Mechanisms of Protection, *Int. J. Mater. Sci.*, 2019, **20**(8), 1912.
9 X.-P. Wang, Q.-X. Wang, H.-P. Lin and N. Chang, Anti-tumor bioactivities of curcumin on mice loaded with gastric carcinoma, *Food Funct.*, 2017, **8**(9), 3319–3326.
10 A. G. Jagtap, S. S. Shirke and A. S. Phadke, Effect of polyherbal formulation on experimental models of inflammatory bowel diseases, *J. Ethnopharmacol.*, 2004, **90**(2–3), 195–204.
11 H. Hatcher, R. Planalp, J. Cho, F. M. Torti and S. V. Torti, Curcumin: From ancient medicine to current clinical trials, *Cell. Mol. Life Sci.*, 2008, **65**(11), 1631–1652.
12 W. Feng, H. Wang, P. Zhang, *et al.*, Modulation of gut microbiota contributes to curcumin-mediated attenuation of hepatic steatosis in rats, *Biochim. Biophys. Acta, Gen. Subj.*, 2017, **1861**(7), 1801–1812.
13 A. Cotillard, S. P. Kennedy, L. C. Kong, *et al.*, Dietary intervention impact on gut microbial gene richness, *Nature*, 2013, **500**(7464), 585–588.
14 S. H. Wong, L. Zhao, X. Zhang, *et al.*, Gavage of Fecal Samples From Patients With Colorectal Cancer Promotes Intestinal Carcinogenesis in Germ-Free and Conventional Mice, *Gastroenterology*, 2017, **153**(6), 1621–1633.e6.
15 E. Saus, S. Iraola-Guzmán, J. R. Willis, A. Brunet-Vega and T. Gabaldón, Microbiome and colorectal cancer: Roles in carcinogenesis and clinical potential, *Mol. Aspects Med.*, 2019, **69**, 93–106.
16 S. H. Wong and J. Yu, Gut microbiota in colorectal cancer: mechanisms of action and clinical applications, *Nat. Rev. Gastroenterol. Hepatol.*, 2019, **16**(11), 690–704.
17 X. Kang, C. Liu, Y. Ding, *et al.*, Roseburia intestinalis generated butyrate boosts anti-PD-1 efficacy in colorectal cancer by activating cytotoxic $CD8^+$ T cells, *Gut*, 2023, (11), 2112–2122.
18 D. Chen, D. Jin, S. Huang, *et al.*, Clostridium butyricum, a butyrate-producing probiotic, inhibits intestinal tumor development through modulating Wnt signaling and gut microbiota, *Cancer Lett.*, 2020, **469**, 456–467.
19 S. Chen, L. Fan, Y. Lin, *et al.*, Bifidobacterium adolescentis orchestrates $CD143^+$ cancer-associated fibroblasts to suppress colorectal tumorigenesis by Wnt signaling-regulated GAS1, *Cancer Commun.*, 2023, **43**(9), 1027–1047.

20 H. Chen, F. Zhang, J. Zhang, X. Zhang, Y. Guo and Q. Yao, A Holistic View of Berberine Inhibiting Intestinal Carcinogenesis in Conventional Mice Based on Microbiome-Metabolomics Analysis, *Front. Immunol.*, 2020, **11**, 588079.
21 J. C. Sedlak, Y. Öh and J. Roper, Metabolism and Colorectal Cancer, *Annu. Rev. Pathol.: Mech. Dis.*, 2023, **18**(1), 467–492.
22 C. Zhang, L. Zhang, Y. Tian, B. Guan and S. Li, Association between metabolic syndrome and early-stage colorectal cancer, *BMC Cancer*, 2023, **23**(1), 1020.
23 Z. Bai, Y. Zhou, Z. Ye, J. Xiong, H. Lan and F. Wang, Tumor-Infiltrating Lymphocytes in Colorectal Cancer: The Fundamental Indication and Application on Immunotherapy, *Front. Immunol.*, 2022, **12**, 808964.
24 A. M. Zaborowski, D. C. Winter and L. Lynch, The therapeutic and prognostic implications of immunobiology in colorectal cancer: a review, *Br. J. Cancer*, 2021, **125**(10), 1341–1349.
25 B.-J. Noh, J. Y. Kwak and D.-W. Eom, Immune classification for the PD-L1 expression and tumour-infiltrating lymphocytes in colorectal adenocarcinoma, *BMC Cancer*, 2020, **20**(1), 58.
26 Y. Lou, J. Zheng, H. Hu, J. Lee and S. Zeng, Application of ultra-performance liquid chromatography coupled with quadrupole time-of-flight mass spectrometry to identify curcumin metabolites produced by human intestinal bacteria, *J. Chromatogr. B:Anal. Technol. Biomed. Life Sci.*, 2015, **985**, 38–47.
27 Z.-Z. Sun, X.-Y. Li, S. Wang, L. Shen and H.-F. Ji, Bidirectional interactions between curcumin and gut microbiota in transgenic mice with Alzheimer's disease, *Appl. Microbiol. Biotechnol.*, 2020, **104**(8), 3507–3515.
28 J. Ma, Y. Deng, M. Zhang and J. Yu, The role of multi-omics in the diagnosis of COVID-19 and the prediction of new therapeutic targets, *Virulence*, 2022, **13**(1), 1101–1110.
29 T. H. Visal, P. Den Hollander, M. Cristofanilli and S. A. Mani, Circulating tumour cells in the -omics era: how far are we from achieving the 'singularity'?, *Br. J. Cancer*, 2022, **127**(2), 173–184.
30 G. Da Violante, N. Zerrouk, I. Richard, *et al.*, Evaluation of the cytotoxicity effect of dimethyl sulfoxide (DMSO) on Caco2/TC7 colon tumor cell cultures, *Biol. Pharm. Bull.*, 2002, **25**(12), 1600–1603.
31 L. Jamalzadeh, H. Ghafoori, *et al.*, Cytotoxic Effects of Some Common Organic Solvents on MCF-7, RAW-264.7 and Human Umbilical Vein Endothelial Cells, *Avicenna J. Med. Biochem.*, 2016, **4**(1), e33453.
32 S. William-Faltaos, D. Rouillard, P. Lechat and G. Bastian, Cell cycle arrest and apoptosis induced by oxaliplatin (L-OHP) on four human cancer cell lines, *Anticancer Res.*, 2006, **26**(3A), 2093–2099.
33 T. Ming, J. Lei, Y. Peng, *et al.*, Curcumin suppresses colorectal cancer by induction of ferroptosis via regulation of p53 and solute carrier family 7 member 11/glutathione/glutathione peroxidase 4 signaling axis, *Phytother. Res.*, 2024, **38**(8), 3954–3972.
34 K. C. Shih, H. W. Chan, C. Y. Wu and H. Y. Chuang, Curcumin Enhances the Abscopal Effect in Mice with Colorectal Cancer by Acting as an Immunomodulator, *Pharmaceutics*, 2023, **15**(5), 1519.
35 R. M. Marjaneh, F. Rahmani, S. M. Hassanian, N. Rezaei, M. Hashemzehi, A. Bahrami, *et al.*, Phytosomal curcumin inhibits tumor growth in colitis-associated colorectal cancer, *J. Cell. Physiol.*, 2018, **233**(10), 6785–6798.
36 H. J. Zhong, Y. P. Zhuang, X. Xie, *et al.*, Washed microbiota transplantation promotes homing of group 3 innate lymphoid cells to the liver via the CXCL16/CXCR6 axis: a potential treatment for metabolic-associated fatty liver disease, *Gut Microbes*, 2024, **16**(1), 2372881.
37 J.-L. Liu, M. Yang, J.-G. Bai, Z. Liu and X.-S. Wang, "Cold" colorectal cancer faces a bottleneck in immunotherapy, *World J. Gastrointest. Oncol.*, 2023, **15**(2), 240–250.
38 Y. Arafat, M. Loft, K. Cao, *et al.*, Current colorectal cancer chemotherapy dosing limitations and novel assessments to personalize treatments, *Aust. N. Z. J. Surg.*, 2022, **92**(11), 2784–2785.
39 S. Choi, E. Lee, B. Akuzum, *et al.*, Melatonin reduces endoplasmic reticulum stress and corneal dystrophy–associated TGFBI p through activation of endoplasmic reticulum–associated protein degradation, *J. Pineal Res.*, 2017, **63**(3), e12426.
40 J. Omwancha, M. D. Anway and T. R. Brown, Differential age–associated regulation of clusterin expression in prostate lobes of brown norway rats, *Prostate*, 2009, **69**(2), 115–125.
41 Z. Mbese, V. Khwaza and B. A. Aderibigbe, Curcumin and Its Derivatives as Potential Therapeutic Agents in Prostate, Colon and Breast Cancers, *Molecules*, 2019, **24**(23), 4386.
42 S. C. Gupta, S. Patchva and B. B. Aggarwal, Therapeutic Roles of Curcumin: Lessons Learned from Clinical Trials, *AAPS J.*, 2013, **15**(1), 195–218.
43 P. Anand, C. Sundaram, S. Jhurani, A. B. Kunnumakkara and B. B. Aggarwal, Curcumin and cancer: An "old-age" disease with an "age-old" solution, *Cancer Lett.*, 2008, **267**(1), 133–164.
44 V. Soleimani, A. Sahebkar and H. Hosseinzadeh, Turmeric (Curcuma longa) and its major constituent (curcumin) as nontoxic and safe substances: Review, *Phytother. Res.*, 2018, **32**(6), 985–995.
45 J. Yan, W. Li, H. Tian, *et al.*, Metal-Phenolic Nanomedicines Regulate T-Cell Antitumor Function for Sono-Metabolic Cancer Therapy, *ACS Nano*, 2023, **17**(15), 14667–14677.
46 B. Hassannia, P. Vandenabeele and T. Vanden Berghe, Targeting Ferroptosis to Iron Out Cancer, *Cancer Cell*, 2019, **35**(6), 830–849.
47 S. J. Dixon, K. M. Lemberg, M. R. Lamprecht, *et al.*, Ferroptosis: An Iron-Dependent Form of Nonapoptotic Cell Death, *Cell*, 2012, **149**(5), 1060–1072.
48 L. Jiang, N. Kon, T. Li, *et al.*, Ferroptosis as a p53-mediated activity during tumour suppression, *Nature*, 2015, **520**(7545), 57–62.

49 B. Hassannia, B. Wiernicki, I. Ingold, *et al.*, Nano-targeted induction of dual ferroptotic mechanisms eradicates high-risk neuroblastoma, *J. Clin. Invest.*, 2018, **128**(8), 3341–3355.
50 Z. Gu, Y. Hao, T. Schomann, F. Ossendorp, P. Ten Dijke and L. J. Cruz, Enhancing anti-tumor immunity through liposomal oxaliplatin and localized immunotherapy via STING activation, *J. Controlled Release*, 2023, **357**, 531–544.
51 Q. Yao, M. Tang, L. Zeng, *et al.*, Potential of fecal microbiota for detection and postoperative surveillance of colorectal cancer, *BMC Microbiol.*, 2021, **21**(1), 156.
52 J. Liu, X. Huang, C. Chen, *et al.*, Identification of colorectal cancer progression-associated intestinal microbiome and predictive signature construction, *J. Transl. Med.*, 2023, **21**(1), 373.
53 J. Q. Fan, W. F. Zhao, Q. W. Lu, F. R. Zha, *et al.*, Fecal microbial biomarkers combined with multi-target stool DNA test improve diagnostic accuracy for colorectal cancer, *World J. Gastrointest. Oncol.*, 2023, **15**(8), 1424–1435.
54 R. Silva-Reis, C. Castro-Ribeiro, M. Gonçalves, *et al.*, An Integrative Approach to Characterize the Early Phases of Dimethylhydrazine-Induced Colorectal Carcinogenesis in the Rat, *Biomedicines*, 2022, **10**(2), 409.
55 C. S. Chang, Y. C. Liao, C. T. Huang, *et al.*, Identification of a gut microbiota member that ameliorates DSS-induced colitis in intestinal barrier enhanced Dusp6-deficient mice, *Cell Rep.*, 2021, **37**(8), 110016.
56 Q. Song, Y. Gao, K. Liu, *et al.*, Gut microbial and metabolomics profiles reveal the potential mechanism of fecal microbiota transplantation in modulating the progression of colitis-associated colorectal cancer in mice, *J. Transl. Med.*, 2024, **22**(1), 1028.
57 M. E. Sanders, D. J. Merenstein, G. Reid, G. R. Gibson and R. A. Rastall, Probiotics and prebiotics in intestinal health and disease: from biology to the clinic, *Nat. Rev. Gastroenterol. Hepatol.*, 2019, **16**(10), 605–616.
58 A. Tiptiri-Kourpeti, K. Spyridopoulou, V. Santarmaki, *et al.*, Lactobacillus casei Exerts Anti-Proliferative Effects Accompanied by Apoptotic Cell Death and Up-Regulation of TRAIL in Colon Carcinoma Cells, *PLoS One*, 2016, **11**(2), e0147960.
59 Y. Yue, S. Wang, J. Shi, *et al.*, Effects of Lactobacillus acidophilus KLDS1.0901 on Proliferation and Apoptosis of Colon Cancer Cells, *Front. Microbiol.*, 2022, **12**, 788040.
60 N. Sugimura, Q. Li, E. S. H. Chu, *et al.*, *Lactobacillus gallinarum* modulates the gut microbiota and produces anti-cancer metabolites to protect against colorectal tumourigenesis, *Gut*, 2022, **71**(10), 2011–2021.
61 K. J. Choi, M. Y. Yoon, J. E. Kim and S. S. Yoon, Gut commensal Kineothrix alysoides mitigates liver dysfunction by restoring lipid metabolism and gut microbial balance, *Sci. Rep.*, 2023, **13**(1), 14668.
62 K. N. Haas and J. L. Blanchard, Kineothrix alysoides, gen. nov., sp. nov., a saccharolytic butyrate-producer within the family Lachnospiraceae, *Int. J. Syst. Evol. Microbiol.*, 2017, **67**(2), 402–410.
63 L. P. Ta, S. Corrigan, C. Tselepis, T. H. Iqbal, C. Ludwig and R. D. Horniblow, Gastrointestinal-inert prebiotic microcomposites improve the growth and community diversity of mucosal-associated bacteria, *J. Controlled Release*, 2024, **375**, 495–512.
64 J. Liu, H. Zhou, Y. Zhang, Y. Huang, W. Fang, Y. Yang, S. Hong, G. Chen, S. Zhao, X. Chen, Z. Zhang, J. Shen, W. Xian, J. Zhan, Y. Zhao, X. Hou, Y. Ma, T. Zhou, H. Zhao and L. Zhang, Docosapentaenoic acid and lung cancer risk: A Mendelian randomization study, *Cancer Med.*, 2019, **8**(4), 1817–1825.
65 M. L. Hartman, M. Rogut, A. Mielczarek-Lewandowska, M. Wozniak and M. Czyz, 17-Aminogeldanamycin Inhibits Constitutive Nuclear Factor-Kappa B (NF-κB) Activity in Patient-Derived Melanoma Cell Lines, *Int. J. Mol. Sci.*, 2020, **21**(11), 3749.
66 A. Mielczarek-Lewandowska, M. Sztiller-Sikorska, M. Osrodek, M. Czyz and M. L. Hartman, 17-Aminogeldanamycin selectively diminishes IRE1α-XBP1s pathway activity and cooperatively induces apoptosis with MEK1/2 and BRAFV600E inhibitors in melanoma cells of different genetic subtypes, *Apoptosis*, 2019, **24**(7–8), 596–611.
67 X. Yang, B. Deng, W. Zhao, Y. Guo, Y. Wan, Z. Wu, S. Su, J. Gu, X. Hu, W. Feng, C. Hu, J. Li, Y. Xu, X. Huang and Y. Lin, FABP5+ lipid-loaded macrophages process tumour-derived unsaturated fatty acid signal to suppress T-cell anti-tumour immunity, *J. Hepatol.*, 2025, **82**(4), 676–689.
68 Y. Xuan, H. Wang, M. M. Yung, F. Chen, W. S. Chan, Y. S. Chan, S. K. Tsui, H. Y. Ngan, K. K. Chan and D. W. Chan, SCD1/FADS2 fatty acid desaturases equipoise lipid metabolic activity and redox-driven ferroptosis in ascites-derived ovarian cancer cells, *Theranostics*, 2022, **12**(7), 3534–3552.
69 Y. Zhang, Y. Sun, S. Song, N. K. Khankari, J. T. Brenna, Y. Shen and K. Ye, Associations of plasma omega-6 and omega-3 fatty acids with overall and 19 site-specific cancers: A population-based cohort study in UK Biobank, *Int. J. Cancer*, 2025, **156**(6), 1154–1172.
70 C. L. Cherbonnel-Lasserre, G. Linares-Cruz, J.-P. Rigaut, L. Sabatier and B. Dutrillaux, Strong decrease in biotin content may correlate with metabolic alterations in colorectal adenocarcinoma, *Int. J. Cancer*, 1997, **72**(5), 768–775.
71 P. Vermonden, M. Vancoppenolle, E. Dierge, E. Mignolet, G. Cuvelier, B. Knoops, M. Page, C. Debier, O. Feron and Y. Larondelle, Punicic Acid Triggers Ferroptotic Cell Death in Carcinoma Cells, *Nutrients*, 2021, **13**(8), 2751.
72 M. Mete, Ü. Üü, I. Aydemir, P. K. Sönmez and M. I. Tuglu, Punicic Acid Inhibits Glioblastoma Migration and Proliferation via the PI3K/AKT1/mTOR Signaling Pathway, *Anti-Cancer Agents Med. Chem.*, 2019, **19**(9), 1120–1131.
73 B. Quitmeyer, C. Emelife, H. Klausner, O. Gbayisomore and S. Phelan, Differential Effects of Punicic Acid on Cytotoxicity and Peroxiredoxin Expression in MCF-7 Breast Cancer and MCF-10A Normal Cells, *Anticancer Res.*, 2024, **44**(11), 4751–4759.

74 R. Zhang, Y. Yang, W. Dong, M. Lin, J. He, X. Zhang, T. Tian, Y. Yang, K. Chen, Q. Y. Lei, S. Zhang, Y. Xu and L. Lv, D-mannose facilitates immunotherapy and radiotherapy of triple-negative breast cancer via degradation of PD-L1, *Proc. Natl. Acad. Sci. U. S. A.*, 2022, **119**(8), e2114851119.

75 N. Iida, A. Dzutsev, C. A. Stewart, *et al.*, Commensal Bacteria Control Cancer Response to Therapy by Modulating the Tumor Microenvironment, *Science*, 2013, **342**(6161), 967–970.

76 B. Routy, E. Le Chatelier, L. Derosa, *et al.*, Gut microbiome influences efficacy of PD-1–based immunotherapy against epithelial tumors, *Science*, 2018, **359**(6371), 91–97.

77 M. Vétizou, J. M. Pitt, R. Daillère, *et al.*, Anticancer immunotherapy by CTLA-4 blockade relies on the gut microbiota, *Science*, 2015, **350**(6264), 1079–1084.

78 X. Kang, C. Liu, Y. Ding, *et al.*, *Roseburia intestinalis* generated butyrate boosts anti-PD-1 efficacy in colorectal cancer by activating cytotoxic CD8 $^{+}$ T cells, *Gut*, 2023, **72**(11), 2112–2122.

79 N. Karin and H. Razon, Chemokines beyond chemo-attraction: CXCL10 and its significant role in cancer and autoimmunity, *Cytokine*, 2018, **109**, 24–28.

80 T. J. Zumwalt, M. Arnold, A. Goel and C. R. Boland, Active secretion of CXCL10 and CCL5 from colorectal cancer microenvironments associates with GranzymeB^{+} CD8^{+} T-cell infiltration, *Oncotarget*, 2015, **6**(5), 2981–2991.

81 U. Barash, Y. Zohar, G. Wildbaum, *et al.*, Heparanase enhances myeloma progression via CXCL10 downregulation, *Leukemia*, 2014, **28**(11), 2178–2187.

82 W. Wang, M. Green, J. E. Choi, *et al.*, CD8^{+} T cells regulate tumour ferroptosis during cancer immunotherapy, *Nature*, 2019, **569**(7755), 270–274.

83 A. Asai and T. Miyazawa, Occurrence of orally administered curcuminoid as glucuronide and glucuronide/sulfate conjugates in rat plasma, *Life Sci.*, 2000, **67**(23), 2785–2793.

84 C. R. Ireson, D. J. Jones, S. Orr, M. W. Coughtrie, D. J. Boocock, M. L. Williams, *et al.*, Metabolism of the cancer chemopreventive agent curcumin in human and rat intestine, *Cancer Epidemiol., Biomarkers Prev.*, 2002, **11**(1), 105–111. PMID: 11815407.

85 M. H. Pan, T. M. Huang and J. K. Lin, Biotransformation of curcumin through reduction and glucuronidation in mice, *Drug Metab. Dispos.*, 1999, **27**(4), 486–494.

86 R. C. Martin, H. S. Aiyer, D. Malik and Y. Li, Effect on pro-inflammatory and antioxidant genes and bioavailable distribution of whole turmeric vs curcumin: Similar root but different effects, *Food Chem. Toxicol.*, 2012, **50**(2), 227–231.

87 G. Peron, S. Sut, S. Dal Ben, D. Voinovich and S. Dall'Acqua, Untargeted UPLC-MS metabolomics reveals multiple changes of urine composition in healthy adult volunteers after consumption of curcuma longa L. extract, *Food Res. Int.*, 2020, **127**, 108730.